MULTISCALE MODEL. SIMUL.
Vol. 22, No. 4, pp. 1608–1645

ASYMPTOTICALLY PROVED NUMERICAL COUPLING OF A 2D FLEXURAL POROUS PLATE WITH THE 3D STOKES FLUID*

MAXIME KRIER†, JULIA ORLIK†, GRIGORY PANASENKO‡, AND KONRAD STEINER†

Abstract. A numerical workflow for a linear multiscale fluid-structure interaction (FSI) problem between 3D Stokes flow and an effective porous, homogenized 2D plate is presented. The underlying effective FSI model is obtained from the method of two-scale convergence for thin perforated and periodic filter structures, performed in earlier works. On the micro scale, the numerical workflow comprises the computation of the filter structure's effective homogenized stiffness tensors utilizing a beam finite element formulation, as well as the computation of the permeability tensor. On the macro scale, a monolithic finite element formulation for the FSI problem with conforming elements is derived. Numerical results and sensitivity studies demonstrating the influence of design variations on the micro scale on the FSI solution are presented for woven filter structures.

Key words. 2D-3D-PDE coupling, fluid-structure interaction, dimension reduction, plate homogenization, Hermite elements, Bogner–Fox–Schmit elements

MSC codes. 35B27, 35J50, 47H05, 74B05, 74K10, 74K20

DOI. 10.1137/23M1627687

1. Introduction.

This paper covers a numerical workflow for an effective 2D-3D model for nonstationary Stokes flow, two-way coupled with a *stiff* elastic, perforated and heterogeneous filter structure of both thickness and period ε. Here, *stiff* refers to a certain contrast in the elastic properties of the structure to the fluid viscosity, which is of order ε^{-3}.

The mathematical model describes the flow-induced displacement of the structure due to jump of fluid stresses across its interface. Such problems are, e.g., of interest in medical modeling of fluid flow through or parallel to (biological) tissue (see, e.g., [43, 34, 16, 28]), as well as in filtration applications with woven and nonwoven filter media (see, e.g., [27, 26, 44, 29]).

Especially in the latter application, state-of-the-art simulation methods typically assume a rigid filter medium. Thereby information on changes of the filter's local surface area and a resulting decreased flow resistance due to the flow-induced displacement are neglected. This neglect may cause significant deviations between simulation results and experimental measurements, especially for flexural filters. Hence, the incorporation of filter displacements into fluid-structure interaction (FSI) models and efficient numerical approaches are of great interest.

Moreover, some of the presented methods are also applicable to the efficient multiscale simulation of textiles and textile-like materials outside of the FSI context.

The considered FSI problem has a multiscale character, with the length scales of the filter structure being significantly smaller than the size of the fluid domain.

*Received by the editors January 2, 2024; accepted for publication (in revised form) September 16, 2024; published electronically December 5, 2024.
https://doi.org/10.1137/23M1627687
Funding: This work was funded by the German Research Foundation under DFG-Project OR 190/6-3.
†Department of Flow and Material Simulation, Fraunhofer ITWM, Kaiserslautern, Germany (maxime.krier@itwm.fraunhofer.de, julia.orlik@itwm.fraunhofer.de, konrad.steiner@itwm.fraunhofer.de).
‡Institute of Applied Mathematics, Vilnius University, Vilnius, Lithuania (grigory.panasenko@univ-st-etienne.fr).

To enable efficient simulations without the need to resolve the microscopic structure in the FSI system, a simultaneous homogenization and dimension reduction approach is considered, replacing the filter by a homogeneous porous 2D plate on the macro scale.

The rigorous asymptotic derivation was performed in [40, 18] for FSI with a connected, permeable, and elastic structure, two-way coupled with Stokes flow. The authors of both articles impose a linearized coupling condition at the fluid-structure interface, namely the continuity of velocities as well as the continuity of normal stresses. Both fluid and structure equations are formulated on fixed, time-independent domains, thereby covering the case of small strains.

Exploiting the same tools as for periodic plates and shells (see, e.g., [39, 23, 25, 24, 38, 21]), the limit system is an immersed 2D plate coupled with 3D Stokes flow in two simple bulk domains. The arising macroscopic model parameters are the three fourth-order homogenized stiffness tensors attained from the same cell problems as in the homogenization and dimension reduction of the elastic structure in [23] outside of the FSI context. In [25] it was shown that these auxiliary cell problems for the linear plate regime in fact coincide with the cell problems for the nonlinear von Karman plate regime.

For the modeling of FSI with textile-like filters consisting of individual yarns, the found cell problems were generalized in [30] to incorporate a linearized contact condition of Robin type between individual yarns adopted from [39].

The derived coupling conditions for the macroscopic FSI problem are nonstandard. The plate's vibration is proportional to the jump of fluid stresses across the plate. The fluid velocity components tangential to the plate are vanishing, while the fluid's velocity and the plate's velocity in normal direction coincide. On both micro and macro scales, the system becomes one-way coupled in steady-state.

Unintuitively, in the macroscopic limit of both FSI systems [40, 18], the homogenized structure is no longer permeable, such that in particular steady-state solutions may no longer exist for commonly encountered simulation setups. For this reason, a phenomenological extension with an interface flux term obeying Darcy's law was proposed and analyzed in [30]. A new macroscopic model parameter, namely the structure's second-order permeability tensor, is introduced. The entries of the permeability tensor are attained from the cell problems of Darcy's law in the fluid part of the periodic unit of the structure; see, e.g., [45].

In the steady-state, the Stokes-Stokes coupling in the proposed poroelastic model resembles so-called Stokes-sieve problems, derived and analyzed, e.g., in [12, 1, 6] and applied, e.g., to the simulation of blood flow through immersed stents in [16]. Moreover, in the nonstationary case, the model may be considered as a simplification of the effective Biot–Kirchhoff-plate systems from [36, 32] and [37, 4], in which the pore-pressure and velocity live in a thin, inflated 3D domain around the 2D plate. Moreover, the authors would like to emphasize previous well-known and related works on Neumann-sieve problems and effective models for the flow through porous layers, such as [10, 2, 32, 35, 7, 33, 19].

The derived numerical approach for the FSI problem is split into two parts. In the first part, the elasticity cell problems for the computation of the filter's stiffness tensors are solved by the finite element (FE) method on the micro scale. Focusing on textile-like filters consisting of slender yarns, a dimension reduction approach from [20] is recalled, allowing the restriction of general elasticity problems on the filter domain to 1D equations on the graph of the yarn centerlines. Utilizing 1D beam FE, the numerical results attained in [39] for the homogenized extensional stiffness tensor are extended to the computation of the homogenized coupling and bending

stiffness tensor. A sensitivity analysis for the influence of changing filter design parameters on the individual tensor entries is performed for a woven filter and the plausibility of attained results is discussed also in regard to the fulfillment of derived theoretical properties.

Furthermore, a numerical method for the computation of the permeability tensor is presented that utilizes a preimplemented microscopic finite volume solver.

In the second phase, the macroscopic FSI system is solved with a monolithic FE formulation, that is, fluid and structure equations are solved as a single system. Input are the precomputed macroscopic tensors of the first phase. For the fluid variables, a formulation with LBB stable FE is proposed. The immersed plate is treated as an interior boundary with globally continuous velocity elements and discontinuous pressure elements at the interface.

For the structure variables, conforming FE are employed. To ensure the H^2-conformity of the plate's deflection, the classical Bogner–Fox–Schmit (BFS) elements [5] are chosen. A similar ansatz was recently formulated in [15] for the interpolation and extension of the displacement of 1D lattice structures to 2D domains if the information on the mixed second-order derivatives is missing. Numerical examples with woven filters are presented and discussed.

2. Model description.

2.1. Multiscale problem. The first section covers a brief summary of the microscopic FSI problem considered in [18, 30], where the emphasis is on the description of the microscopic textile-like filter structure. The interested reader is referred to the cited articles for further details.

The nonstationary Stokes flow through a channel is considered. The latter is separated in half along the x_3-direction by a thin, flexural, textile-like filter, which is fixed at its outer edges. The filter itself is of a deterministic nature and possesses a small period ε in the in-plane direction $\bar{x} = (x_1, x_2)$, while its thickness in the x_3-direction is of the same order as ε. Here and in the following, the x_3-direction is referred to as the normal direction.

With these assumptions, the filter domain can be most efficiently described by the periodic repetition of a reference cell $Y_\varepsilon^s = \varepsilon Y^s \subset \mathbb{R}^3$ in the in-plane direction. The set Y_ε^s is contained within a reference cell εY, where $Y = (0,1)^2 \times (-\frac{1}{2}, \frac{1}{2})$ is referred to as the unit cell. The spatial variable in the reference and unit cell is denoted by y, respectively.

It is assumed that Y_ε^s is the disjoint union of finitely many Lipschitz domains, such that the interior of the closure of Y_ε^s is a connected set. Here, each Lipschitz domain is representing an individual yarn. The union of shared boundaries of the Lipschitz domains is denoted by $S_{Y,\varepsilon}^c = \varepsilon S_Y^c$. It represents the contact surfaces between individual yarns. Furthermore, the complement $Y_\varepsilon^f = \varepsilon Y^f$ with $Y^f = Y_\varepsilon \setminus \overline{Y_\varepsilon^s}$ is assumed to be a connected Lipschitz domain. It is occupied with viscous fluid in the microscopic FSI model. An illustration of the introduced domains is provided in Figure 1.

By finite periodic repetition of Y_ε^s, one attains a microscopic structure domain, denoted by $\Omega_\varepsilon^{M,s}$, which is fully contained within a membrane domain

$$\Omega_\varepsilon^M = (0, L_1) \times (0, L_2) \times \left(-\frac{\varepsilon}{2}, \frac{\varepsilon}{2}\right).$$

The spatial variable in Ω_ε^M is denoted by x.

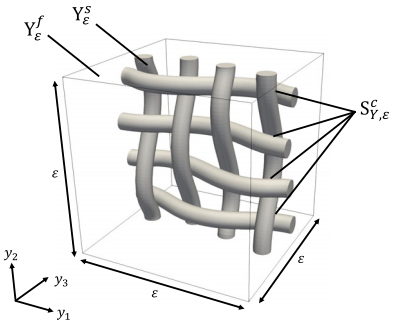

FIG. 1. *Example of a reference cell for a twill woven filter.*

The contact surfaces, attained by periodic repetition of $S^c_{Y,\varepsilon}$, are denoted by S^c_ε. Furthermore, it is assumed that the filter is fixed at its outer edges, given by the set

$$\partial^{\mathrm{fix}}\Omega^{M,s}_\varepsilon = \partial\Omega^M_\varepsilon \cap \partial\Omega^{M,s}_\varepsilon,$$

assumed to be of nonzero measure and disjoint from the planes $\{x_3 = \pm\frac{\varepsilon}{2}\}$. The remaining boundary of $\Omega^{M,s}_\varepsilon$ is given by

$$\partial^{\mathrm{fs}}\Omega^{M,s}_\varepsilon = \partial\Omega^{M,s}_\varepsilon \setminus (\partial^{\mathrm{fix}}\Omega^{M,s}_\varepsilon \cup S^c_\varepsilon).$$

The microscopic displacement $\boldsymbol{u}_\varepsilon\colon (0,T)\times\Omega^{M,s}_\varepsilon \to \mathbb{R}^3$ of the filter structure is governed by linear elasticity with Robin-type contact conditions; see [39, 30]. The governing system reads

$$\begin{aligned}
\rho_s\partial_{tt}\boldsymbol{u}_\varepsilon - \nabla\cdot(\underline{\boldsymbol{A}}^\varepsilon D(\boldsymbol{u}_\varepsilon)) &= \boldsymbol{g}_\varepsilon && \text{in } (0,T)\times\Omega^{M,s}_\varepsilon,\\
\boldsymbol{u}_\varepsilon &= \boldsymbol{0} && \text{on } (0,T)\times\partial^{\mathrm{fix}}\Omega^{M,s}_\varepsilon,\\
[\![\underline{\boldsymbol{A}}^\varepsilon D(\boldsymbol{u}_\varepsilon)]\!]\boldsymbol{\eta} &= \boldsymbol{0} && \text{on } (0,T)\times S^c_\varepsilon,\\
(\underline{\boldsymbol{A}}^\varepsilon D(\boldsymbol{u}_\varepsilon))\,\boldsymbol{\eta} &= \frac{1}{\varepsilon}\boldsymbol{R}^\varepsilon[\![\boldsymbol{u}_\varepsilon]\!] && \text{on } (0,T)\times S^c_\varepsilon
\end{aligned} \tag{2.1}$$

with solid density ρ_s and initial conditions $\boldsymbol{u}_\varepsilon(0) = \boldsymbol{0}, \partial_t\boldsymbol{u}_\varepsilon(0) = \boldsymbol{0}$.

Here, $D(\boldsymbol{u}) = \frac{1}{2}(\nabla\boldsymbol{u} + (\nabla\boldsymbol{u})^T)$ denotes the symmetric gradient, $\underline{\boldsymbol{A}}^\varepsilon = \underline{\boldsymbol{A}}(x/\varepsilon)$ with $\underline{\boldsymbol{A}} \in L^\infty_\#(Y^s)^{3\times3\times3\times3}$ denotes the fourth-order material stiffness tensor, and $\boldsymbol{R}^\varepsilon = \boldsymbol{R}(x/\varepsilon)$ with $\boldsymbol{R} \in L^\infty_\#(S^c_\varepsilon)^{3\times3}$ is a Robin matrix modeling contacts between individual yarns.

The term

$$[\![\boldsymbol{u}_\varepsilon]\!](x) = \lim_{\lambda\downarrow0}(\boldsymbol{u}_\varepsilon(x+\lambda\boldsymbol{\eta}) - \boldsymbol{u}_\varepsilon(x-\lambda\boldsymbol{\eta})), \quad x \in S^c_\varepsilon,$$

for an arbitrary but fixed normal vector $\boldsymbol{\eta}$ on the interior boundary S^c_ε is the jump of displacements. Hence, in the case of *glued yarns,* that is, $\boldsymbol{R}^\varepsilon \to \infty$, problem (2.1) coincides with a classical elasticity problem on a single connected domain.

In (2.1) and the following, the product between a fourth-order tensor $\underline{\boldsymbol{A}} \in \mathbb{R}^{n\times n\times n\times n}$ and a square matrix $\boldsymbol{B} \in \mathbb{R}^{n\times n}$ is written as

$$\underline{\boldsymbol{A}}\boldsymbol{B} = \left(\sum_{k,l=1}^{n} a_{ijkl} b_{kl} \right)_{i,j=1}^{n} \in \mathbb{R}^{n\times n}.$$

In the microscopic setting, the membrane domain Ω_ε^M is extended by the two bulk domains

$$(0, L_1) \times (0, L_2) \times \left(-L_3 - \frac{\varepsilon}{2}, -\frac{\varepsilon}{2}\right),$$
$$(0, L_1) \times (0, L_2) \times \left(\frac{\varepsilon}{2}, L_3 + \frac{\varepsilon}{2}\right),$$

in which the standard nonstationary Stokes flow is described. At the fluid-structure interface $\partial^{\mathrm{fs}}\Omega_\varepsilon^{M,s}$, linearized coupling conditions are prescribed, that is, continuity of velocity and continuity of normal stresses; see [18, 30].

The following main assumptions on the stiffness tensor are standard for the modeling with linear elasticity. They are required for the existence and uniqueness of a weak solution to the microscopic problem under appropriate regularity of the initial conditions and the right-hand sides; see [30] for a proof. Here and in what follows, $\boldsymbol{A} : \boldsymbol{B}$ denotes the standard Frobenius inner product between two square matrices.

Assumption 2.1. The tensor $\underline{\boldsymbol{A}} = (a_{ijkl})_{i,j,k,l=1}^3$ is symmetric, i.e., $a_{ijkl} = a_{jikl} = a_{klij}$ almost everywhere in Y^s, and coercive on the space of symmetric matrices, i.e., there exists a constant $\underline{c} > 0$ such that for all symmetric matrices $\boldsymbol{P} \in \mathbb{R}^{3\times 3}$ one has $(\underline{\boldsymbol{A}}\boldsymbol{P}) : \boldsymbol{P} \geq \underline{c}(\boldsymbol{P} : \boldsymbol{P})$.

Furthermore, the Robin condition matrix $\boldsymbol{R}$ is symmetric and positive definite almost everywhere.

Example 2.2. As an example, the contact condition can be modeled by the matrix

$$\boldsymbol{R} = \boldsymbol{\eta} \otimes \boldsymbol{\eta} + \gamma_{\mathrm{friction}}(\boldsymbol{I} - \boldsymbol{\eta} \otimes \boldsymbol{\eta})$$

with the normal vector $\boldsymbol{\eta}$, where $\gamma_{\mathrm{friction}} > 0$ is a penalization friction parameter for jumps of tangential displacements.

2.2. Macroscopic model description. Based on the rigorously derived macroscopic FSI problems from [40, 18] by considering the scale limit $\varepsilon \to 0$ with simultaneous homogenization and dimension reduction, an extended, phenomenological macroscopic model for the considered FSI problem was proposed and analyzed in [30]. The extension comprises the inclusion of the linearized contact conditions between yarns from the previous section and an additional flow resistance term in the macroscopic FSI setting. Note that a rigorous derivation of the permeable interface condition by asymptotic methods is still ongoing research.

In the proposed macroscopic model, nonstationary Stokes flow is prescribed in two disjoint fluid domains,

$$\Omega^- = (0, L_1) \times (0, L_2) \times (-L_3, 0),$$
$$\Omega^+ = (0, L_1) \times (0, L_2) \times (0, L_3),$$

that is

$$\begin{aligned} \rho_f \partial_t \boldsymbol{v}^\pm - 2\mu \nabla \cdot D(\boldsymbol{v}^\pm) + \nabla p^\pm &= \boldsymbol{f}^\pm \qquad \text{in } (0,T) \times \Omega^\pm, \\ \nabla \cdot \boldsymbol{v}^\pm &= 0 \qquad \text{in } (0,T) \times \Omega^\pm \end{aligned} \tag{2.2}$$

with fluid density ρ_f, dynamic viscosity μ, and some volume force density $\boldsymbol{f}^{\pm}$. Moreover, the entire model domain is denoted by

$$\Omega = (0, L_1) \times (0, L_2) \times (-L_3, L_3).$$

The Stokes equations (2.2) are accompanied by Dirichlet and zero-stress boundary conditions on the bottom, top, and lateral boundaries,

$$\begin{aligned} \partial^{\text{in}}\Omega &= (0, L_1) \times (0, L_2) \times \{-L_3\}, \\ \partial^{\text{out}}\Omega &= (0, L_1) \times (0, L_2) \times \{L_3\}, \\ \partial^{\text{no-slip}}\Omega &= \partial\Omega \setminus (\partial^{\text{in}}\Omega \cup \partial^{\text{out}}\Omega). \end{aligned}$$

The boundary conditions of choice read

$$\begin{aligned} \boldsymbol{v}^- &= \boldsymbol{0} && \text{on } (0,T) \times \partial^{\text{in}}\Omega, \\ (2\mu D(\boldsymbol{v}^+) - p\boldsymbol{I})\boldsymbol{e}_3 &= \boldsymbol{0} && \text{on } (0,T) \times \partial^{\text{out}}\Omega, \\ \boldsymbol{v}^{\pm} &= \boldsymbol{0} && \text{on } (0,T) \times \partial^{\text{no-slip}}\Omega, \end{aligned} \tag{2.3}$$

where $\boldsymbol{I}$ is the 3×3 unit matrix and $\boldsymbol{e}_i$ denotes the ith unit vector. The inflow condition is chosen as zero for simplicity; otherwise additional regularity and extension properties of the inflow condition are required that enable the lifting of the respective solution space.

The two fluid domains are separated by the interior boundary

$$\Sigma = (0, L_1) \times (0, L_2) \times \{0\},$$

on which the fluid velocity is assumed to be continuous, that is, $\boldsymbol{v}^-|_\Sigma = \boldsymbol{v}^+|_\Sigma$. The in-plane variable on Σ is denoted by $\bar{x} = (x_1, x_2)$.

The interface represents the mean-plane of the filter structure, whose in-plane displacement $\bar{\boldsymbol{u}}$ and outer-plane deflection u_3 are governed by the Kirchhoff plate equations

$$\begin{aligned} -\nabla_{\bar{x}} \cdot (\underline{\boldsymbol{A}}^{\text{hom}} D_{\bar{x}}(\bar{\boldsymbol{u}}) + \underline{\boldsymbol{B}}^{\text{hom}} \nabla_{\bar{x}}^2 u_3) &= \boldsymbol{0} && \text{on } (0,T) \times \Sigma, \\ \hat{\rho}_s \partial_{tt} u_3 + \nabla_{\bar{x}}^2 : (\underline{\boldsymbol{B}}^{\text{hom}} D_{\bar{x}}(\bar{\boldsymbol{u}}) + \underline{\boldsymbol{C}}^{\text{hom}} \nabla_{\bar{x}}^2 u_3) &= [\![2\mu D(\boldsymbol{v}) - p\boldsymbol{I}]\!]\boldsymbol{e}_3 \cdot \boldsymbol{e}_3 + g_3 && \text{on } (0,T) \times \Sigma \end{aligned} \tag{2.4}$$

with clamped boundary conditions

$$\begin{aligned} \bar{\boldsymbol{u}} &= \boldsymbol{0} && \text{on } (0,T) \times \partial\Sigma, \\ u_3 = \nabla_{\bar{x}} u_3 \cdot \boldsymbol{\eta} &= 0 && \text{on } (0,T) \times \partial\Sigma. \end{aligned} \tag{2.5}$$

Here, the expression

$$[\![2\mu D(\boldsymbol{v}) - p\boldsymbol{I}]\!] = (2\mu D(\boldsymbol{v}^+) - p^+\boldsymbol{I})|_\Sigma - (2\mu D(\boldsymbol{v}^-) - p^-\boldsymbol{I})|_\Sigma$$

denotes the jump of fluid stresses. The operators $\nabla_{\bar{x}}, D_{\bar{x}}, \nabla_{\bar{x}}^2$ are the respective differential operators with respect to the in-plane variables and g_3 is some surface force density.

Furthermore, the entries of the homogenized fourth-order stiffness tensors $\underline{\boldsymbol{A}}^{\mathrm{hom}}$, $\underline{\boldsymbol{B}}^{\mathrm{hom}}, \underline{\boldsymbol{C}}^{\mathrm{hom}} \in \mathbb{R}^{2\times2\times2\times2}$ are attained by averaging of elasticity cell solutions $\boldsymbol{\chi}_{ij}^{M}$ and $\boldsymbol{\chi}_{ij}^{B}, i,j=1,2$, reading

(2.6)
$$
\begin{aligned}
a_{ijkl}^{\mathrm{hom}} &= \frac{1}{|Y^s|}\left[\left(\underline{\boldsymbol{A}}\left(D(\boldsymbol{\chi}_{ij}^{M})+\boldsymbol{M}^{ij}\right), D(\boldsymbol{\chi}_{kl}^{M})+\boldsymbol{M}^{kl}\right)_{Y^s} + \left(\boldsymbol{R}[\![\boldsymbol{\chi}_{ij}^{M}]\!], [\![\boldsymbol{\chi}_{kl}^{M}]\!]\right)_{S^c}\right],\\
b_{ijkl}^{\mathrm{hom}} &= \frac{1}{|Y^s|}\left[\left(\underline{\boldsymbol{A}}\left(D(\boldsymbol{\chi}_{ij}^{B})-y_3\boldsymbol{M}^{ij}\right), D(\boldsymbol{\chi}_{kl}^{M})+\boldsymbol{M}^{kl}\right)_{Y^s} + \left(\boldsymbol{R}[\![\boldsymbol{\chi}_{ij}^{B}]\!], [\![\boldsymbol{\chi}_{kl}^{M}]\!]\right)_{S^c}\right],\\
c_{ijkl}^{\mathrm{hom}} &= \frac{1}{|Y^s|}\left[\left(\underline{\boldsymbol{A}}\left(D(\boldsymbol{\chi}_{ij}^{B})-y_3\boldsymbol{M}^{ij}\right), D(\boldsymbol{\chi}_{kl}^{B})-y_3\boldsymbol{M}^{kl}\right)_{Y^s} + \left(\boldsymbol{R}[\![\boldsymbol{\chi}_{ij}^{B}]\!], [\![\boldsymbol{\chi}_{kl}^{B}]\!]\right)_{S^c}\right]
\end{aligned}
$$

for $i,j,k,l \in \{1,2\}$ and $\boldsymbol{M}^{ij} = \frac{1}{2}(\boldsymbol{e}_i \otimes \boldsymbol{e}_j + \boldsymbol{e}_j \otimes \boldsymbol{e}_i) \in \mathbb{R}^{3\times3}$.

The cell solutions solve so-called membrane and bending cell problems. In variational formulation, these are to find $\boldsymbol{\chi}_{ij}^{M,B} \in H^1_{\#,0}(Y^s)^3$ such that

$$
\begin{aligned}
&\left(\underline{\boldsymbol{A}}\left(D(\boldsymbol{\chi}_{ij}^{M})+\boldsymbol{M}^{ij}\right), D(\boldsymbol{X})\right)_{Y^s} + \left(\boldsymbol{R}[\![\boldsymbol{\chi}_{ij}^{M}]\!], [\![\boldsymbol{X}]\!]\right)_{S^c} = 0,\\
&\left(\underline{\boldsymbol{A}}\left(D(\boldsymbol{\chi}_{ij}^{B})-y_3\boldsymbol{M}^{ij}\right), D(\boldsymbol{X})\right)_{Y^s} + \left(\boldsymbol{R}[\![\boldsymbol{\chi}_{ij}^{B}]\!], [\![\boldsymbol{X}]\!]\right)_{S^c} = 0
\end{aligned}
\tag{2.7}
$$

for all $\boldsymbol{X} \in H^1_{\#,0}(Y^s)^3$. Here, $H^1_{\#,0}(Y^s)$ is the broken Sobolev space of Y-periodic functions, that is, functions whose restrictions to the individual Lipschitz domains, that Y^s is comprised of, are elements of the usual Sobolev space, and which are additionally 1-periodic in the in-plane direction, with vanishing mean-value in Y^s. Since $\boldsymbol{M}^{ij} = \boldsymbol{M}^{ji}$, one can verify that there are a total of six independent cell problems.

The tensors $\underline{\boldsymbol{A}}^{\mathrm{hom}}, \underline{\boldsymbol{B}}^{\mathrm{hom}}, \underline{\boldsymbol{C}}^{\mathrm{hom}}$ are commonly referred to as extensional, coupling, and bending stiffness tensors. Formally speaking, the entries of $\underline{\boldsymbol{A}}^{\mathrm{hom}}$ determine the resistance of the structure to in-plane loads, such as applied tension and shearing, while the entries of $\underline{\boldsymbol{C}}^{\mathrm{hom}}$ describe the resistance to bending and torsional loads. Additional coupling between in-plane strain and outer-plane bending is introduced by the entries of $\underline{\boldsymbol{B}}^{\mathrm{hom}}$.

Last, the macroscopic model parameter

$$
\hat{\rho}_s = \frac{\delta}{|Y_\varepsilon|}\int_{Y_\varepsilon^s} \rho_s \,\mathrm{d}y
$$

is the averaged solid density ρ_s, with δ denoting the characteristic thickness of the structure.

As an additional coupling condition between fluid equations (2.2) and structure equations (2.4), flow-resistivity is modeled by a Darcy interface term

$$
\mu\delta\boldsymbol{K}^{-1}(\boldsymbol{v}^+ - \partial_t u_3 \boldsymbol{e}_3) = [\![2\mu D(\boldsymbol{v}) - p\boldsymbol{I}]\!]\boldsymbol{e}_3 \quad \text{on } (0,T)\times\Sigma \tag{2.8}
$$

with resistivity tensor $\boldsymbol{K}^{-1} \in \mathbb{R}^{3\times3}$, chosen as the inverse of the permeability tensor $\boldsymbol{K}$. The entries of $\boldsymbol{K}$ are given by

$$
k_{ij} = \frac{1}{|Y^f|}(\nabla\boldsymbol{\omega}_i, \nabla\boldsymbol{\omega}_j)_{Y^f}, \tag{2.9}
$$

where $\boldsymbol{\omega}_i, i \in \{1,2,3\}$, are a solution to the Darcy fluid cell problems. In variational formulation, these are to find

$$
\boldsymbol{\omega}_i \in H^1_{\mathrm{per,div}}(Y^f) = \{\boldsymbol{W} \in H^1(Y^f)^3 : \boldsymbol{W} \text{ is periodic}, \nabla\cdot\boldsymbol{W} = 0, \boldsymbol{W} = \boldsymbol{0} \text{ on } \partial Y^s\}
$$

such that

$$(\nabla \boldsymbol{\omega}_i, \nabla \boldsymbol{W})_{Y^f} = (\boldsymbol{e}_i, \boldsymbol{W})_{Y^f} \tag{2.10}$$

for all $\boldsymbol{W} \in H^1_{\mathrm{per,div}}(Y^f)$; see, e.g., Chapter 7 of [45]. For the extreme case $\boldsymbol{K} \to \boldsymbol{0}$, the interface Σ becomes impermeable and the normal fluid velocity component coincides with the normal velocity of the plate. The tangential fluid velocity components vanish. One attains the FSI model derived in [18]. For the other case $\boldsymbol{K} \to \infty$, the interface is no longer seen by the fluid and the jump of fluid stresses vanishes. One attains regular Stokes flow in the entire domain Ω.

For easier notation, the variable $\hat{\boldsymbol{K}} = \mu^{-1}\delta^{-1}\boldsymbol{K}$ is introduced.

Summarizing, the macroscopic FSI problem reads

$$\begin{aligned}
\rho_f \partial_t \boldsymbol{v}^{\pm} - 2\mu \nabla \cdot D(\boldsymbol{v}^{\pm}) + \nabla p^{\pm} &= \boldsymbol{f}^{\pm} && \text{in } (0,T)\times\Omega^{\pm},\\
\nabla \cdot \boldsymbol{v}^{\pm} &= 0 && \text{in } (0,T)\times\Omega^{\pm},\\
\boldsymbol{v}^{-} &= \boldsymbol{0} && \text{on } (0,T)\times\partial^{\mathrm{in}}\Omega,\\
(2\mu D(\boldsymbol{v}^{+}) - p\boldsymbol{I})\boldsymbol{e}_3 &= \boldsymbol{0} && \text{on } (0,T)\times\partial^{\mathrm{out}}\Omega,\\
\boldsymbol{v}^{\pm} &= \boldsymbol{0} && \text{on } (0,T)\times\partial^{\text{no-slip}}\Omega,\\
\boldsymbol{v}^{-} &= \boldsymbol{v}^{+} && \text{on } (0,T)\times\Sigma,\\
-\nabla_{\bar{x}} \cdot (\underline{\boldsymbol{A}}^{\mathrm{hom}} D_{\bar{x}}(\bar{\boldsymbol{u}}) + \underline{\boldsymbol{B}}^{\mathrm{hom}} \nabla^2_{\bar{x}} u_3) &= \boldsymbol{0} && \text{on } (0,T)\times\Sigma,\\
\hat{\rho}_s \partial_{tt} u_3 + \nabla^2_{\bar{x}} : (\underline{\boldsymbol{B}}^{\mathrm{hom}} D_{\bar{x}}(\bar{\boldsymbol{u}}) + \underline{\boldsymbol{C}}^{\mathrm{hom}} \nabla^2_{\bar{x}} u_3) & \\
= [\![2\mu D(\boldsymbol{v}) - p\boldsymbol{I}]\!]\boldsymbol{e}_3 \cdot \boldsymbol{e}_3 + g_3 && \text{on } (0,T)\times\Sigma,\\
\hat{\boldsymbol{K}}^{-1}(\boldsymbol{v}^{+} - \partial_t u_3 \boldsymbol{e}_3) = [\![2\mu D(\boldsymbol{v}) - p\boldsymbol{I}]\!]\boldsymbol{e}_3 && \text{on } (0,T)\times\Sigma,\\
\bar{\boldsymbol{u}} &= \boldsymbol{0} && \text{on } (0,T)\times\partial\Sigma,\\
u_3 = \nabla_{\bar{x}} u_3 \cdot \boldsymbol{\eta} &= 0 && \text{on } (0,T)\times\partial\Sigma,
\end{aligned} \tag{2.11}$$

accompanied with the initial conditions $\boldsymbol{v}^{\pm}(0) = \boldsymbol{0}, u_3(0) = \partial_t u_3(0) = 0$.

The steady-state formulation of system (2.11) consists of the Stokes-Stokes coupling

$$\begin{aligned}
-2\mu \nabla \cdot D(\boldsymbol{v}^{\pm}) + \nabla p^{\pm} &= \boldsymbol{f}^{\pm} && \text{in } \Omega^{\pm},\\
\nabla \cdot \boldsymbol{v}^{\pm} &= 0 && \text{in } \Omega^{\pm},\\
\boldsymbol{v}^{-} &= \boldsymbol{v}^{\mathrm{in}} && \text{on } \partial^{\mathrm{in}}\Omega,\\
(2\mu D(\boldsymbol{v}^{+}) - p\boldsymbol{I})\boldsymbol{e}_3 &= \boldsymbol{0} && \text{on } \partial^{\mathrm{out}}\Omega,\\
\boldsymbol{v}^{\pm} &= \boldsymbol{0} && \text{on } \partial^{\text{no-slip}}\Omega,\\
\boldsymbol{v}^{-} &= \boldsymbol{v}^{+} && \text{on } \Sigma,\\
\hat{\boldsymbol{K}}^{-1}\boldsymbol{v}^{+} &= [\![2\mu D(\boldsymbol{v}) - p\boldsymbol{I}]\!]\boldsymbol{e}_3 && \text{on } \Sigma,
\end{aligned} \tag{2.12}$$

one-way coupled to the Kirchhoff plate

$$\begin{aligned}
-\nabla_{\bar{x}} \cdot (\underline{\boldsymbol{A}}^{\mathrm{hom}} D_{\bar{x}}(\bar{\boldsymbol{u}}) + \underline{\boldsymbol{B}}^{\mathrm{hom}} \nabla^2_{\bar{x}} u_3) &= \boldsymbol{0} && \text{on } \Sigma,\\
\nabla^2_{\bar{x}} : (\underline{\boldsymbol{B}}^{\mathrm{hom}} D_{\bar{x}}(\bar{\boldsymbol{u}}) + \underline{\boldsymbol{C}}^{\mathrm{hom}} \nabla^2_{\bar{x}} u_3) &= [\![2\mu D(\boldsymbol{v}) - p\boldsymbol{I}]\!]\boldsymbol{e}_3 \cdot \boldsymbol{e}_3 + g_3 && \text{on } \Sigma,\\
\bar{\boldsymbol{u}} &= \boldsymbol{0} && \text{on } \partial\Sigma,\\
u_3 = \nabla_{\bar{x}} u_3 \cdot \boldsymbol{\eta} &= 0 && \text{on } \partial\Sigma.
\end{aligned} \tag{2.13}$$

The Stokes-Stokes coupling (2.12) is actually reminiscent of the system presented in [16] for the modeling of immersed, rigid stents in blood flow. The cited model is based on classical Stokes-sieve problems analyzed, e.g., in [12].

For completeness, some fundamental results are recalled from the literature, that suffice for the well-posedness of the system; see [30] and references therein. The discussion starts with the homogenized structure.

LEMMA 2.3. *For each $i,j \in \{1,2\}$, there exists a unique cell solution $\boldsymbol{\chi}_{ij}^{M,B} \in H^1_{\#,0}(Y^s)^3$ to the cell problems* (2.7)*, respectively.*

As a consequence, one can verify the following lemma; see also Theorem 2 in [23].

LEMMA 2.4. *The homogenized stiffness tensors given by the expressions* (2.6) *are well-defined. The induced bilinear form*

$$a^{hom}((\bar{\boldsymbol{u}},u_3),(\bar{\boldsymbol{U}},U_3)) = (\underline{\boldsymbol{A}}^{hom} D_{\bar{x}}(\bar{\boldsymbol{u}}), D_{\bar{x}}(\bar{\boldsymbol{U}}))_\Sigma + (\underline{\boldsymbol{B}}^{hom} D_{\bar{x}}(\bar{\boldsymbol{u}}), \nabla^2_{\bar{x}} U_3)_\Sigma + (\underline{\boldsymbol{B}}^{hom} \nabla^2_{\bar{x}} u_3, D_{\bar{x}}(\bar{\boldsymbol{U}}))_\Sigma + (\underline{\boldsymbol{C}}^{hom} \nabla^2_{\bar{x}} u_3, \nabla^2_{\bar{x}} U_3)_\Sigma$$

is continuous and bounded on $H^1_0(\Sigma)^2 \times H^2_0(\Sigma)$. The induced norm

$$\|(\bar{\boldsymbol{u}},u_3)\|^2_{hom} = a^{hom}((\bar{\boldsymbol{u}},u_3),(\bar{\boldsymbol{u}},u_3))$$

is equivalent to the standard norm on $H^1_0(\Sigma)^2 \times H^2_0(\Sigma)$. The tensors $\underline{\boldsymbol{A}}^{hom}$ and $\underline{\boldsymbol{C}}^{hom}$ share the same symmetry properties as $\underline{\boldsymbol{A}}$ and are coercive on the space of symmetric matrices.

Additionally, one can find the proof of the following statement on the permeability tensor, e.g., in Chapter 7 of [45].

PROPOSITION 2.5. *For each $i \in \{1,2,3\}$, the fluid cell problems* (2.10) *have a unique solution $\boldsymbol{\omega}_i \in H^1_{per,div}(Y^f)$. The expressions* (2.9) *are well-defined and the resulting permeability tensor $\boldsymbol{K} \in \mathbb{R}^{3\times 3}$ is symmetric and positive definite.*

The statements are sufficient to verify the existence of solutions to the presented FSI problem, e.g., by a standard Galerkin approach employing Rothe's method. A detailed proof is given in [30] based on the framework from [37].

PROPOSITION 2.6. *Let $\boldsymbol{f}^\pm \in L^2((0,T),L^2(\Omega^\pm)^3), g_3 \in L^2((0,T),L^2(\Sigma))$. Let further the assumptions of Lemma* 2.3 *be satisfied. Then the system* (2.11) *has a unique pressure-free solution $(\boldsymbol{v},\bar{\boldsymbol{u}},u_3), \boldsymbol{v}|_{\Omega^\pm} = \boldsymbol{v}^\pm$ with*

$$\begin{aligned}
&\boldsymbol{v} \in L^2((0,T),\mathcal{V}_{div}) \cap L^\infty((0,T),L^2(\Omega^- \cup \Omega^+)^3),\\
&\bar{\boldsymbol{u}} \in L^2((0,T),H^1_0(\Sigma)^2),\\
&u_3 \in L^\infty((0,T),H^2_0(\Sigma)),\ \text{with } \partial_t u_3 \in L^\infty((0,T),L^2(\Sigma)),
\end{aligned}$$

where

$$\begin{aligned}
\mathcal{V}_{div} &= \{\boldsymbol{v} \in \mathcal{V} : \nabla \cdot \boldsymbol{v} = 0 \text{ in } \Omega^- \cup \Omega^+\},\\
\mathcal{V} &= \{\boldsymbol{v} \in H^1(\Omega^- \cup \Omega^+)^3 : \boldsymbol{v} = \boldsymbol{0} \text{ on } \partial^{in}\Omega \cup \partial^{no\text{-}slip}\Omega\}.
\end{aligned}$$

One can additionally verify that the well-posedness of the FSI system is still granted when one switches from constant stiffness and permeability tensors to the natural choice of tensors with L^∞-regularity on Σ. For this purpose it is necessary to assume that the coercivity and symmetry from Lemma 2.4 and Proposition 2.5 remain valid for the generalized tensors.

Last, by inspecting the plate equations (2.4), it is clear that $\bar{\boldsymbol{u}}$ vanishes whenever the coupling stiffness tensor $\underline{\boldsymbol{B}}^{\mathrm{hom}}$ is zero. In fact, this latter condition is frequently met under symmetry assumptions on the structure Y^s and the model parameters $\underline{\boldsymbol{A}}$ and $\boldsymbol{R}$; see Lemma 6.9 in [25]. Hence, the main displacement variable of interest is the plate's deflection.

3. Numerical methods.

3.1. Computation of the homogenized stiffness tensors. In this section, an overview on the numerical computation of the homogenized stiffness tensors $\underline{\boldsymbol{A}}^{\mathrm{hom}}$, $\underline{\boldsymbol{B}}^{\mathrm{hom}}$, $\underline{\boldsymbol{C}}^{\mathrm{hom}}$ is given. For the textile-like structures in mind, an efficient dimension reduction approach with 1D beam FEs, generalized by the incorporation of contact conditions, is presented in [39] for the computation of $\underline{\boldsymbol{A}}^{\mathrm{hom}}$. The extension to the computation of $\underline{\boldsymbol{B}}^{\mathrm{hom}}$ and $\underline{\boldsymbol{C}}^{\mathrm{hom}}$ is presented here.

For implementation of the cell problems (2.7) with FEM, it proves to be beneficial to introduce the perturbation functions $\boldsymbol{S}_{ij}^{M,B} \in C^\infty(Y)^3$ as

$$
\begin{aligned}
&\boldsymbol{S}_{11}^{M}(y) = \begin{pmatrix} y_1 \\ 0 \\ 0 \end{pmatrix}, \quad \boldsymbol{S}_{12}^{M}(y) = \frac{1}{2}\begin{pmatrix} y_2 \\ y_1 \\ 0 \end{pmatrix}, \quad \boldsymbol{S}_{22}^{M}(y) = \begin{pmatrix} 0 \\ y_2 \\ 0 \end{pmatrix}, \\
&\boldsymbol{S}_{11}^{B}(y) = \frac{1}{2}\begin{pmatrix} -2y_1y_3 \\ 0 \\ y_1^2 \end{pmatrix}, \quad \boldsymbol{S}_{12}^{B}(y) = \frac{1}{2}\begin{pmatrix} -y_2y_3 \\ -y_1y_3 \\ y_1y_2 \end{pmatrix}, \quad \boldsymbol{S}_{22}^{B}(y) = \frac{1}{2}\begin{pmatrix} 0 \\ -2y_2y_3 \\ y_2^2 \end{pmatrix},
\end{aligned} \tag{3.1}
$$

which are chosen as analytical solutions of the differential equations

$$
D(\boldsymbol{S}_{ij}^{M}) = \boldsymbol{M}^{ij}, \quad D(\boldsymbol{S}_{ij}^{B}) = -y_3\boldsymbol{M}^{ij} \quad \text{in } Y^s, \quad [\![\boldsymbol{S}_{ij}^{M,B}]\!] = \boldsymbol{0} \quad \text{on } S^c \tag{3.2}
$$

for $i,j = 1,2$. The choice of $\boldsymbol{S}_{ij}^{M,B}$ with the stated properties is not uniquely determined but every function satisfying (3.2) is suitable for what follows.

By defining the perturbated cell solutions $\boldsymbol{m}_{ij}^{M,B} = \boldsymbol{\chi}_{ij}^{M,B} + \boldsymbol{S}_{ij}^{M,B} \in H^1(Y^s)^3$, one attains the equivalent cell problem formulations

$$
\Big(\underline{\boldsymbol{A}}D(\boldsymbol{m}_{ij}^{M,B}), D(\boldsymbol{X})\Big)_{Y^s} + \Big(\boldsymbol{R}[\![\boldsymbol{m}_{ij}^{M,B}]\!], [\![\boldsymbol{X}]\!]\Big)_{S^c} = 0 \tag{3.3}
$$

for all $\boldsymbol{X} \in H^1_{\#}(Y^s)^3$, with the perturbated periodicity condition that $\boldsymbol{m}_{ij}^{M,B} - \boldsymbol{S}_{ij}^{M,B}$ are Y-periodic. The solution of the above formulation is unique up to an additive constant, since the vanishing mean value in the solution space is dropped. It is intuitive to interpret the perturbated cell solutions as actual displacement fields on Y^s.

The computation of the homogenized tensor entries (2.6) with the perturbated cell solutions in the continuous setting becomes

$$
\begin{aligned}
a_{ijkl}^{\mathrm{hom}} &= \frac{1}{|Y^s|}\Big[\big(\underline{\boldsymbol{A}}D(\boldsymbol{m}_{ij}^{M}), D(\boldsymbol{m}_{kl}^{M})\big)_{Y^s} + \big(\boldsymbol{R}[\![\boldsymbol{m}_{ij}^{M}]\!], [\![\boldsymbol{m}_{kl}^{M}]\!]\big)_{S^c}\Big], \\
b_{ijkl}^{\mathrm{hom}} &= \frac{1}{|Y^s|}\Big[\big(\underline{\boldsymbol{A}}D(\boldsymbol{m}_{ij}^{B}), D(\boldsymbol{m}_{kl}^{M})\big)_{Y^s} + \big(\boldsymbol{R}[\![\boldsymbol{m}_{ij}^{B}]\!], [\![\boldsymbol{m}_{kl}^{M}]\!]\big)_{S^c}\Big], \\
c_{ijkl}^{\mathrm{hom}} &= \frac{1}{|Y^s|}\Big[\big(\underline{\boldsymbol{A}}D(\boldsymbol{m}_{ij}^{B}), D(\boldsymbol{m}_{kl}^{B})\big)_{Y^s} + \big(\boldsymbol{R}[\![\boldsymbol{m}_{ij}^{B}]\!], [\![\boldsymbol{m}_{kl}^{B}]\!]\big)_{S^c}\Big].
\end{aligned} \tag{3.4}
$$

As can be seen, the uniqueness of $\boldsymbol{m}_{ij}^{M,B}$ up to an additive constant is sufficient in (3.4), since the functions only appear in gradient and jump terms.

For completeness, sufficient conditions for a vanishing coupling stiffness tensor are recalled from Lemma 6.9 in [25]. In [3], the same proof strategy was used to prove orthotropy, transversal symmetry, and isotropy for 3D periodic and symmetric elastic structures. The stated conditions are met for typical woven filters made out of a homogeneous, isotropic material.

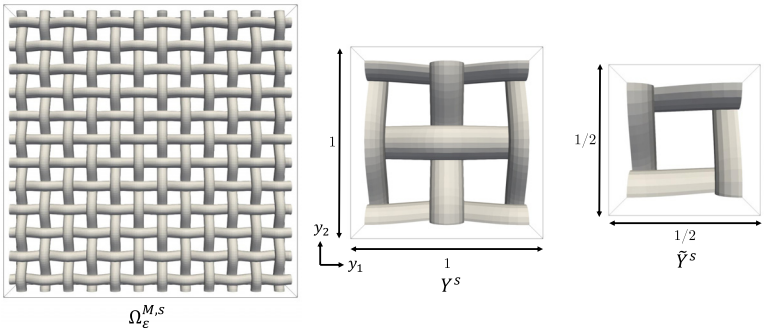

FIG. 2. *Illustration of the structure domain $\Omega_\varepsilon^{M,s}$ (left), solid part of unit cell Y^s (center), and quarter of the unit cell $\tilde{Y}^s$ (right) for a plain woven filter.*

PROPOSITION 3.1. *Let Y^s be symmetric w.r.t. the planes $\{y_1 = \frac{1}{2}\}$ and $\{y_2 = \frac{1}{2}\}$ in the sense that the transformations*

$$\mathbf{T}_1 \colon Y^s \to Y^s, \quad y \mapsto (1-y_1)\boldsymbol{e}_1 + y_2\boldsymbol{e}_2 + y_3\boldsymbol{e}_3,$$
$$\mathbf{T}_2 \colon Y^s \to Y^s, \quad y \mapsto y_1\boldsymbol{e}_1 + (1-y_2)\boldsymbol{e}_2 + y_3\boldsymbol{e}_3$$

are well-defined.

Let $\tilde{Y}^s$ denote the restriction of Y^s to a quarter of the unit cell $(0,\frac{1}{2})^2 \times (-\frac{1}{2},\frac{1}{2})$. Assume that $\tilde{Y}^s$ is rotational-symmetric w.r.t. the diagonal axis $\{y_1 = y_2, y_3 = 0\}$ and $\{y_1 = y_2 = \frac{1}{4}\}$ in the sense that the transformations

$$\mathbf{T}_3 \colon \tilde{Y}^s \to \tilde{Y}^s, \quad y \mapsto y_2\boldsymbol{e}_1 + y_1\boldsymbol{e}_2 - y_3\boldsymbol{e}_3,$$
$$\mathbf{T}_4 \colon \tilde{Y}^s \to \tilde{Y}^s, \quad y \mapsto \left(\frac{1}{2} - y_2\right)\boldsymbol{e}_1 + y_1\boldsymbol{e}_2 + y_3\boldsymbol{e}_3$$

are well-defined.

Then one has $\underline{\boldsymbol{B}}^{hom} = \mathbf{0}$, as well as the additional symmetry

$$a^{hom}_{1111} = a^{hom}_{2222}, \quad c^{hom}_{1111} = c^{hom}_{2222}.$$

Example 3.2. As the most frequently encountered example in filtration, a plain woven filter is considered. The domains of Proposition 3.1 are illustrated in Figure 2.

For the discrete formulation with 1D beam elements, it is assumed that each Lipschitz domain Ω in Y^s can be described as a curved rod of length L with constant cross-section of characteristic size $r > 0$. That is, there exists a smooth curve

$$\boldsymbol{\gamma} \colon [0, L] \to \mathbb{R}^3, \quad s_1 \mapsto \boldsymbol{\gamma}(s_1), \quad \int_0^L |\boldsymbol{\gamma}'(s_1)| \, \mathrm{d}s_1 = L$$

parameterized by its arc-length with well-defined Frenet–Serret frame

$$\boldsymbol{t}(s_1) = \boldsymbol{\gamma}'(s_1), \quad \boldsymbol{n}(s_1) = \frac{\boldsymbol{t}'(s_1)}{|\boldsymbol{t}'(s_1)|}, \quad \boldsymbol{b}(s_1) = \boldsymbol{t}(s_1) \times \boldsymbol{n}(s_1)$$

such that

$$\Omega = \{\boldsymbol{\Phi}(s) = \boldsymbol{\gamma}(s_1) + s_2\boldsymbol{n}(s_1) + s_3\boldsymbol{b}(s_1) : s = (s_1, s_2, s_3) \in (0, L) \times \omega_r\},$$

where $\omega_r = r\omega \subset \mathbb{R}^2$ is a Lipschitz domain centered around $\mathbf{0}$.

Under the above assumption, the dimension reduction approach from section 3 of [20] allows the restriction of displacement fields on Ω to a so-called elementary displacement along the curve $\boldsymbol{\gamma}$, i.e., the centerline of the yarn.

DEFINITION 3.3. *Let $\boldsymbol{u} \in L^1(\Omega)^3$ be given, which (with slight abuse of notation) is interpreted as a function of $s = (s_1, s_2, s_3) \in (0, L) \times \omega_r$ by considering $\boldsymbol{u} \circ \boldsymbol{\Phi}$. Its elementary displacement is defined as*

$$\boldsymbol{u}_e(s) = \boldsymbol{U}(s_1) + \boldsymbol{R}(s_1) \times (s_2 \boldsymbol{n}(s_1) + s_3 \boldsymbol{b}(s_1)), \tag{3.5}$$

where

$$\begin{aligned}
\boldsymbol{U}(s_1) &= \frac{1}{r^2|\omega|} \int_{\omega_r} \boldsymbol{u}(s_1, s_2, s_3)\, \mathrm{d}(s_2, s_3), \\
\boldsymbol{R}(s_1) \cdot \boldsymbol{t}(s_1) &= \frac{1}{(I_2 + I_3) r^4} \int_{\omega_r} ((s_2 \boldsymbol{n}(s_1) + s_3 \boldsymbol{b}(s_1)) \times \boldsymbol{u}(s)) \cdot \boldsymbol{t}(s_1)\, \mathrm{d}(s_2, s_3), \\
\boldsymbol{R}(s_1) \cdot \boldsymbol{n}(s_1) &= \frac{1}{I_3 r^4} \int_{\omega_r} ((s_2 \boldsymbol{n}(s_1) + s_3 \boldsymbol{b}(s_1)) \times \boldsymbol{u}(s)) \cdot \boldsymbol{n}(s_1)\, \mathrm{d}(s_2, s_3), \\
\boldsymbol{R}(s_1) \cdot \boldsymbol{b}(s_1) &= \frac{1}{I_2 r^4} \int_{\omega_r} ((s_2 \boldsymbol{n}(s_1) + s_3 \boldsymbol{b}(s_1)) \times \boldsymbol{u}(s)) \cdot \boldsymbol{b}(s_1)\, \mathrm{d}(s_2, s_3)
\end{aligned} \tag{3.6}$$

and $I_k = \int_\omega s_k\, \mathrm{d}(s_2, s_3), k = 2, 3$, are moments of area.

Here, $\boldsymbol{a} \times \boldsymbol{b}$ denotes the standard cross-product in $\mathbb{R}^3$. The representation (3.5) can be understood as a displacement of the yarn centerline with an additional rotation of the yarn cross-section along the centerline. The remainder term

$$\boldsymbol{u}_w = \boldsymbol{u} - \boldsymbol{u}_e$$

is commonly referred to as the warping term and can be interpreted as the deformation of the cross-section. In practical application, it is assumed to be small in comparison to the elementary displacement for slender structures. In fact, one has the following a priori estimate from Theorem 3.1 in [20].

PROPOSITION 3.4. *Let $\boldsymbol{u} \in H^1(\Omega)^3$ and let $\boldsymbol{u}_e, \boldsymbol{u}_w$ denote its elementary displacement and the corresponding warping term, respectively. There exists $\overline{r} > 0$, solely dependent on ω and $\boldsymbol{\gamma}$, such that there exist a uniform constant $\overline{c} > 0$ with*

$$\begin{aligned}
\|\nabla \boldsymbol{u}_w\|_{L^2(\Omega)} &\le \overline{c} \|D(\boldsymbol{u})\|_{L^2(\Omega)}, \\
\|\boldsymbol{u}_w\|_{L^2(\Omega)} &\le \overline{c} r \|D(\boldsymbol{u})\|_{L^2(\Omega)}, \\
r\|\boldsymbol{R}'\|_{L^2((0,L))} + \|\boldsymbol{U}' - \boldsymbol{R} \times \boldsymbol{t}\|_{L^2((0,L))} &\le \frac{\overline{c}}{r} \|D(\boldsymbol{u})\|_{L^2(\Omega)}
\end{aligned}$$

for all $r < \overline{r}$. Here, $\boldsymbol{R}', \boldsymbol{U}'$ denote the first-order derivatives with respect to s_1.

By discretizing each yarn centerline $\boldsymbol{\gamma}$ by a finite sequence of piecewise linear segments, one attains a 1D frame structure with a sequence of nodes denoted by $(\boldsymbol{n}_1, \ldots, \boldsymbol{n}_m)$. The frame structure serves as a 1D FE mesh with the associated nodal DOF corresponding to the three centerline displacements $\boldsymbol{U}$ and the three rotations $\boldsymbol{R}$ from (3.6), respectively. The interpolation method of choice is standard 1D beam elements in 3D space with 12 DOF per element; see, e.g., Chapter 5 of [31].

The method is extended in [39] by the introduction of contact node pairs $(\boldsymbol{n}_i, \boldsymbol{n}_j)$ in between two yarns, serving as an approximation of the Robin-type interface condition. For an extensive discussion of the assembly of the stiffness matrix and numerical

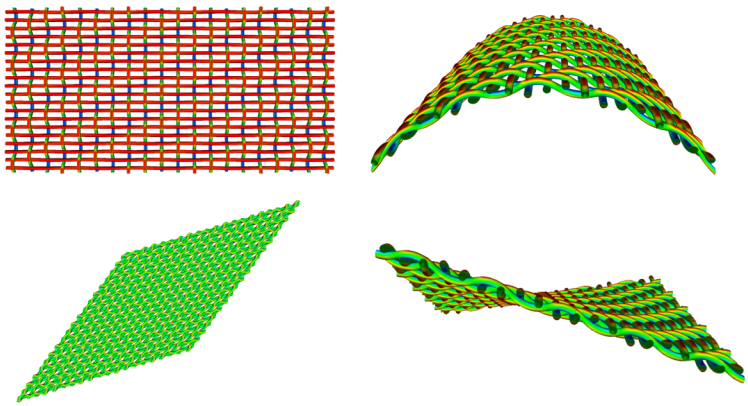

FIG. 3. *Perturbated cell solutions* $\boldsymbol{m}_{11}^M, \boldsymbol{m}_{11}^B$ *(top) and* $\boldsymbol{m}_{12}^M, \boldsymbol{m}_{12}^B$ *(bottom) interpreted as displacement fields of a twill woven filter. Colors indicate local stresses.*

analysis of the method for general linear elasticity problems, the reader is referred to [39].

For the incorporation of the perturbated Y-periodic boundary conditions, an augmented master-slave approach is employed. It requires the evaluation of the FE interpolation of the perturbation functions $\boldsymbol{S}_{ij}^{M,B}$ in each periodic node pair $(\boldsymbol{n}_1, \boldsymbol{n}_2)$ on the lateral boundaries of Y^s, respectively.

The resulting numerical solving routine of the cell problems and the computation of the stiffness tensor entries is implemented in the FiberFEM solver of the textile simulation software TexMath [17].

Example 3.5. As commonly encountered examples in real-world filtration application, the perturbated cell solutions for a twill woven filter are presented in Figure 3. The remaining two solutions are given by rotational symmetry of the filter. For illustration purposes, the periodic unit was repeated five times in each in-plane direction.

3.2. Computation of the permeability tensor. The computation of the permeability tensor $\boldsymbol{K}$ is performed by standard means, utilizing a voxel discretization of the filter structure attained from TexMath. The common approach is actually not to solve the provided cell problems (2.10), but to perform an approximation procedure based on Darcy's law. The computational effort for both approaches is expected to be comparable.

The methodology starts by performing three (stationary) Stokes flow simulations in a fully resolved reference cell with a prescribed constant pressure drop $[\![p_i]\!] \in \mathbb{R}, i = 1, 2, 3$, along the main axes, respectively. For the remaining boundaries, periodic boundary conditions are applied.

In a next step, from the attained solutions $(\boldsymbol{v}_i, p_i)$, the average velocities $\hat{\boldsymbol{v}}_i \in \mathbb{R}^3, i = 1, 2, 3$, are computed. Afterward, by approximating the pressure gradient by the finite difference

$$\nabla p_i \approx \frac{[\![p_i]\!]}{L_i} \boldsymbol{e}_i \in \mathbb{R}^3$$

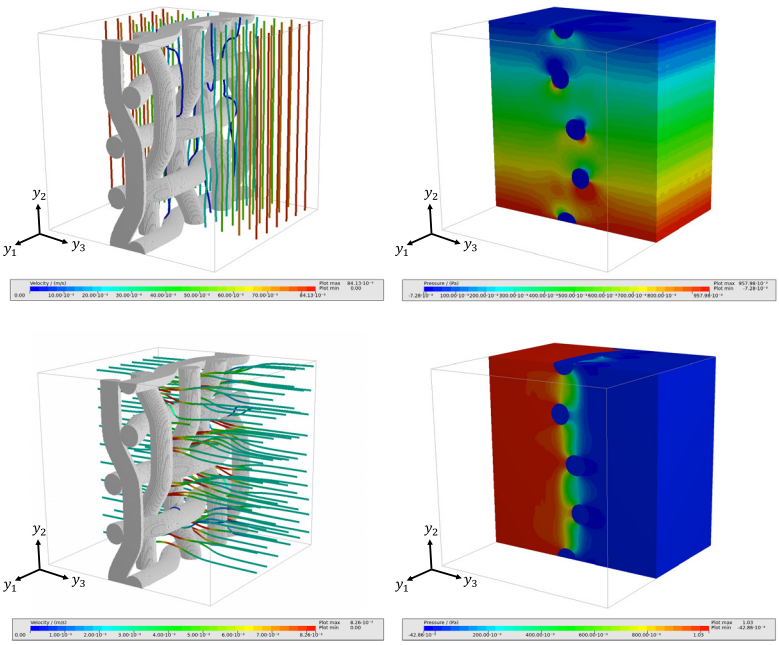

FIG. 4. *Flow solutions* $(\boldsymbol{v}_2, p_2)$ *(top) and* $(\boldsymbol{v}_3, p_3)$ *(bottom) for a twill woven filter. The remaining flow solution is of a similar nature due to symmetry of the structure.*

with L_i denoting the respective physical length of the structure in the x_i-direction, one can approximate $\boldsymbol{K}$ by the solution of the system of linear equations

$$\hat{\boldsymbol{v}}_i = -\frac{[\![p_i]\!]}{L_i \mu} \boldsymbol{K} \boldsymbol{e}_i, \quad i = 1, 2, 3,$$

under the assumption that Darcy's law applies. In the considered case, $L_3 = \delta$ is the characteristic thickness of the filter and the remaining lengths are given by the period ε.

By linearity, the computed tensor $\boldsymbol{K}$ is independent of the choice of $[\![p_i]\!]$, as well as μ. Exemplary flow solutions $(\boldsymbol{v}_i, p_i)$ for a twill woven filter with $[\![p_i]\!] = 1$ Pa and $\mu = 1 \times 10^{-3}$ Pa s are presented in Figure 4. They are attained utilizing the LIR-Stokes solver of the software GeoDict.

3.3. Monolithic FSI solver. The numerical method to solve the FSI system (2.11) consists of two phases. In the first phase, the macroscopic model parameters $\underline{\boldsymbol{A}}^{\mathrm{hom}}, \underline{\boldsymbol{B}}^{\mathrm{hom}}, \underline{\boldsymbol{C}}^{\mathrm{hom}}$, as well as $\boldsymbol{K}$, are computed utilizing the microscopic routines from the previous two sections. Afterward, a monolithic FE discretization of (2.11) is employed, that is, fluid and structure equations are solved as a single discrete system.

For the derivation of the FE system, the auxiliary variable $w_3 = \partial_t u_3$ for the plate's normal velocity is introduced. Furthermore, the required space-variable-dependent function space is denoted by

$$\mathcal{Y} = \mathcal{V} \times L^2(\Omega^- \cup \Omega^+) \times H_0(\Sigma)^2 \times H_0^2(\Sigma) \times L^2(\Sigma).$$

With this notation, Rothe's method is employed for the semidiscretization of system (2.11) in time. For this purpose, let $[\Delta t^{n+1}] = t^{n+1} - t^n$ with discrete time steps

$0 = t^0 < t^1 < \cdots < t^N = T$ for some $N \geq 1$. The approximation of partial derivatives in time is performed via backward difference quotients

$$\partial_t u(t^{n+1}) \approx \frac{u^{n+1} - u^n}{[\Delta t^{n+1}]}$$

for purely space-dependent functions $\boldsymbol{y}^n = (\boldsymbol{v}^n, p^n, \bar{\boldsymbol{u}}^n, u_3^n, w_3^n) \in \mathcal{Y}$, approximating the solution at time t^n. For $n = 0$, the approximation is given by the initial data.

For the right-hand-side functions, the semidiscretization in time reads

$$\boldsymbol{f}^{n+1} = \frac{1}{[\Delta t^{n+1}]} \int_{t^n}^{t^{n+1}} \boldsymbol{f}(\tau)\, \mathrm{d}\tau, \quad g_3^{n+1} = \frac{1}{[\Delta t^{n+1}]} \int_{t^n}^{t^{n+1}} g_3(\tau)\, \mathrm{d}\tau.$$

Standard procedure delivers the variational formulation. For step $n+1$, the semidiscretized formulation of system (2.11) is to find $\boldsymbol{y}^{n+1} = (\boldsymbol{v}^{n+1}, p^{n+1}, \bar{\boldsymbol{u}}^{n+1}, u_3^{n+1}, w_3^{n+1}) \in \mathcal{Y}$ such that

$$\begin{aligned}
&\frac{\rho_f}{[\Delta t^{n+1}]}(\boldsymbol{v}^{n+1}, \boldsymbol{V})_{\Omega^- \cup \Omega^+} + 2\mu(D(\boldsymbol{v}^{n+1}), D(\boldsymbol{V}))_{\Omega^- \cup \Omega^+} - (p^{n+1}, \nabla \cdot \boldsymbol{V})_{\Omega^- \cup \Omega^+} \\
&\quad + (\hat{\boldsymbol{K}}^{-1} \boldsymbol{v}^{n+1}, \boldsymbol{V})_\Sigma - \frac{1}{[\Delta t^{n+1}]}(\hat{\boldsymbol{K}}^{-1} u_3^{n+1} \boldsymbol{e}_3, \boldsymbol{V})_\Sigma \\
&= (\boldsymbol{f}^{n+1}, \boldsymbol{V})_{\Omega^- \cup \Omega^+} + \frac{\rho_f}{[\Delta t^{n+1}]}(\boldsymbol{v}^n, \boldsymbol{V})_{\Omega^- \cup \Omega^+} - \frac{1}{[\Delta t^{n+1}]}(\hat{\boldsymbol{K}}^{-1} u_3^n \boldsymbol{e}_3, \boldsymbol{V})_\Sigma, \\
&\quad - (\nabla \cdot \boldsymbol{v}^{n+1}, P)_{\Omega^- \cup \Omega^+} = 0, \\
&\frac{\hat{\rho}_s}{[\Delta t^{n+1}]}(w_3^{n+1}, U_3)_\Sigma + a^{\mathrm{hom}}((\bar{\boldsymbol{u}}^{n+1}, u_3^{n+1}), (\bar{\boldsymbol{U}}, U_3)) - (\hat{\boldsymbol{K}}^{-1} \boldsymbol{v}^{n+1}, U_3 \boldsymbol{e}_3)_\Sigma \\
&\quad + \frac{1}{[\Delta t^{n+1}]}(\hat{\boldsymbol{K}}^{-1} u_3^{n+1} \boldsymbol{e}_3, U_3 \boldsymbol{e}_3)_\Sigma \\
&= (g_3^{n+1}, U_3)_\Sigma + \frac{\hat{\rho}_s}{[\Delta t^{n+1}]}(w_3^n, U_3)_\Sigma + \frac{1}{[\Delta t^{n+1}]}(\hat{\boldsymbol{K}}^{-1} u_3^n \boldsymbol{e}_3, U_3 \boldsymbol{e}_3)_\Sigma, \\
&\hat{\rho}_s(w_3^{n+1}, W_3)_\Sigma - \frac{\hat{\rho}_s}{[\Delta t^{n+1}]}(u_3^{n+1}, W_3)_\Sigma = -\frac{\hat{\rho}_s}{[\Delta t^{n+1}]}(u_3^n, W_3)_\Sigma
\end{aligned} \tag{3.7}$$

for all $(\boldsymbol{V}, P, \bar{\boldsymbol{U}}, U_3, W_3) \in \mathcal{Y}$.

Utilizing Lemma 2.4 and Proposition 2.5, the well-posedness of (3.7) follows with the classical LBB theorem.

THEOREM 3.6. *For all $n = 0, \ldots, N-1$, the semidiscrete system* (3.7) *has a unique solution $\boldsymbol{y}^{n+1}$.*

Proof. For easier notation, it is assumed that all arising scalar constants, apart from $[\Delta t^{n+1}]$, are equal to 1. Furthermore, the superscript $n+1$ is omitted whenever it is clear from context.

The proof is performed by induction. Let n be given. With the assumptions above and after introducing the scaled test functions $[\Delta t]\boldsymbol{V}$ and $[\Delta t]P$, system (3.7) can be abstracted to

$$\begin{aligned}
a(\boldsymbol{\phi}, \boldsymbol{\Phi}) + b(\boldsymbol{\Phi}, p) &= L[\boldsymbol{\Phi}], \\
b(\boldsymbol{\phi}, P) &= 0,
\end{aligned}$$

where $\boldsymbol{\phi} = (\boldsymbol{v}, \bar{\boldsymbol{u}}, u_3, w_3), \boldsymbol{\Phi} = (\boldsymbol{V}, \bar{\boldsymbol{U}}, U_3, W_3)$, L is the bounded linear functional

$$\begin{aligned} L[\boldsymbol{\Phi}] = {} & (\boldsymbol{f}^{n+1}, \boldsymbol{V})_{\Omega^- \cup \Omega^+} + \frac{\rho_f}{[\Delta t]}(\boldsymbol{v}^n, \boldsymbol{V})_{\Omega^- \cup \Omega^+} - \frac{1}{[\Delta t]}(\hat{\boldsymbol{K}}^{-1} u_3^n \boldsymbol{e}_3, \boldsymbol{V})_\Sigma \\ & + (g_3^{n+1}, U_3)_\Sigma + \frac{\hat{\rho}_s}{[\Delta t]}(w_3^n, U_3)_\Sigma + \frac{1}{[\Delta t]}(\hat{\boldsymbol{K}}^{-1} u_3^n \boldsymbol{e}_3, U_3 \boldsymbol{e}_3)_\Sigma \\ & - \frac{\hat{\rho}_s}{[\Delta t]}(u_3^n, W_3)_\Sigma \end{aligned}$$

with solutions from previous time steps treated as given data, and

$$\begin{aligned} a(\boldsymbol{\phi}, \boldsymbol{\Phi}) = {} & (\boldsymbol{v}, \boldsymbol{V})_{\Omega^- \cup \Omega^+} + [\Delta t](D(\boldsymbol{v}), D(\boldsymbol{V}))_{\Omega^- \cup \Omega^+} + [\Delta t](\hat{\boldsymbol{K}}^{-1} \boldsymbol{v}, \boldsymbol{V})_\Sigma \\ & - (\hat{\boldsymbol{K}}^{-1} u_3 \boldsymbol{e}_3, \boldsymbol{V})_\Sigma + [\Delta t]^{-1}(w_3, U_3)_\Sigma + a^{\mathrm{hom}}((\bar{\boldsymbol{u}}, u_3), (\bar{\boldsymbol{U}}, U_3)) \\ & - (\hat{\boldsymbol{K}}^{-1} \boldsymbol{v}, U_3 \boldsymbol{e}_3)_\Sigma + [\Delta t]^{-1}(\hat{\boldsymbol{K}}^{-1} u_3 \boldsymbol{e}_3, U_3 \boldsymbol{e}_3)_\Sigma + (w_3, W_3)_\Sigma \\ & - [\Delta t]^{-1}(u_3, W_3)_\Sigma, \\ b(\boldsymbol{\phi}, P) = {} & -[\Delta t](\nabla \cdot \boldsymbol{v}, P)_{\Omega^- \cup \Omega^+}. \end{aligned}$$

Similar to classical Stokes theory, the coercivity of the bilinear form a can be ensured on the entirety of $\mathcal{V} \times H_0^1(\Sigma)^2 \times H_0^2(\Sigma) \times L^2(\Sigma)$ with Lemma 2.4 and Proposition 2.5, since

$$\begin{aligned} a(\boldsymbol{\phi}, \boldsymbol{\phi}) = {} & \|\boldsymbol{v}\|^2_{L^2(\Omega^- \cup \Omega^+)} + [\Delta t]\|D(\boldsymbol{v})\|^2_{L^2(\Omega^- \cup \Omega^+)} \\ & + \|\hat{\boldsymbol{K}}^{-\frac{1}{2}}([\Delta t]^{\frac{1}{2}} v_3 - [\Delta t]^{-\frac{1}{2}} u_3 \boldsymbol{e}_3)\|^2_{L^2(\Sigma)} \\ & + \|(\bar{\boldsymbol{u}}, u_3)\|^2_{\mathrm{hom}} + \|w_3\|^2_{L^2(\Sigma)}, \end{aligned}$$

where $\hat{\boldsymbol{K}}^{-\frac{1}{2}}$ denotes the unique square root of $\hat{\boldsymbol{K}}^{-1}$. In particular, a is coercive on the kernel of b.

Again from classical Stokes theory, one can further deduce that independent of the choice of $(\bar{\boldsymbol{u}}, u_3, w_3)$, there exists a constant $\underline{c} > 0$ such that for all $p|_{\Omega^\pm}$ with $p \in \mathcal{P}$ the LBB condition

$$\sup_{\substack{\boldsymbol{v} \in \mathcal{V} \\ \boldsymbol{v}|_{\Omega^\pm} \neq \boldsymbol{0}}} \frac{(\nabla \cdot \boldsymbol{v}|_{\Omega^\pm}, p|_{\Omega^\pm})_{\Omega^\pm}}{\|\boldsymbol{v}\|_{H^1(\Omega^\pm)}} \geq \underline{c}\|p\|_{L^2(\Omega^\pm)} \tag{3.8}$$

for each subdomain $\Omega^\pm$ is fulfilled. The statement then follows by inductive application of the LBB theorem. ∎

With the established existence of solutions in the semidiscrete setting, the system (3.7) is further discretized with respect to the space variable. For this purpose, conforming FE are chosen, i.e., one chooses finite dimensional approximation spaces

$$\mathcal{V}^h \subset \mathcal{V}, \quad \mathcal{P}^h \subset L^2(\Omega^- \cup \Omega^+), \quad \bar{\mathcal{U}}^h \subset H_0^1(\Sigma)^2, \quad \mathcal{U}_3^h \subset H_0^2(\Sigma), \quad \mathcal{W}_3^h \subset L^2(\Sigma)$$

and sets $\mathcal{Y}^h = \mathcal{V}^h \times \mathcal{P}^h \times \bar{\mathcal{U}}^h \times \mathcal{U}_3^h \times \mathcal{W}_3^h$. Here and in the following, h denotes a characteristic element size for spatial decomposition of the computational domain Ω.

In what follows, let

$$(\{\boldsymbol{V}_k^h\}, \{P_k^h\}, \{\bar{\boldsymbol{U}}_k^h\}, \{U_{3\,k}^h\}, \{W_{3\,k}^h\})$$

form a basis of $\mathcal{Y}^h$ and let further

$$\boldsymbol{y}^{n,h} = (\boldsymbol{v}^{n,h}, p^{n,h}, \bar{\boldsymbol{u}}^{n,h}, u_3^{n,h}, w_3^{n,h})^T \in \mathcal{Y}^h$$

be an approximation of $\boldsymbol{y}^n \in \mathcal{Y}$. The semidiscrete solution variable $\boldsymbol{y}^{n,h}$ is associated with its DOF vector, also denoted by $\boldsymbol{y}^{n,h}$.

With this notation, $\boldsymbol{y}^{n+1,h}$ is the solution to

$$\left(\frac{1}{[\Delta t^{n+1}]}\boldsymbol{S}_1 + \boldsymbol{S}_2\right)\boldsymbol{y}^{n+1,h} = \frac{1}{[\Delta t^{n+1}]}\boldsymbol{S}_1\boldsymbol{y}^{n,h} + \boldsymbol{L}(t^{n+1}) \tag{3.9}$$

with the system matrices

$$\boldsymbol{S}_1 := \begin{pmatrix} \boldsymbol{M}_{VV} & 0 & 0 & -\boldsymbol{R}_{VU} & 0 \\ 0 & 0 & 0 & 0 & 0 \\ 0 & 0 & 0 & 0 & 0 \\ 0 & 0 & 0 & \boldsymbol{R}_{UU} & \boldsymbol{M}_{UW} \\ 0 & 0 & 0 & -\boldsymbol{M}_{UW}^T & 0 \end{pmatrix},$$

$$\boldsymbol{S}_2 := \begin{pmatrix} \boldsymbol{A} + \boldsymbol{R}_{VV} & -\boldsymbol{B}^T & 0 & 0 & 0 \\ -\boldsymbol{B} & 0 & 0 & 0 & 0 \\ 0 & 0 & \boldsymbol{P}_A & \boldsymbol{P}_{B_1} & 0 \\ -\boldsymbol{R}_{VU}^T & 0 & \boldsymbol{P}_{B_2} & \boldsymbol{P}_C & 0 \\ 0 & 0 & 0 & 0 & \boldsymbol{M}_{WW} \end{pmatrix}$$

consisting of the constant block matrices

$$\begin{aligned}
\boldsymbol{M}_{VV} &= \left(\rho_f(\boldsymbol{V}_k^h, \boldsymbol{V}_l^h)_{\Omega^-\cup\Omega^+}\right)_{kl}, & \boldsymbol{M}_{UW} &= \left(\hat{\rho}_s(U_{3k}^h, W_{3l}^h)_\Sigma\right)_{kl}, \\
\boldsymbol{M}_{WW} &= \left(\hat{\rho}_s(W_{3k}^h, W_{3l}^h)_\Sigma\right)_{kl}, & \boldsymbol{R}_{VV} &= \left((\hat{\boldsymbol{K}}^{-1}\boldsymbol{V}_k^h, \boldsymbol{V}_l^h)_\Sigma\right)_{kl}, \\
\boldsymbol{R}_{VU} &= \left((\hat{\boldsymbol{K}}^{-1}\boldsymbol{V}_k^h, U_{3l}^h\boldsymbol{e}_3)_\Sigma\right)_{kl}, & \boldsymbol{R}_{UU} &= \left((\hat{\boldsymbol{K}}^{-1}U_{3k}^h\boldsymbol{e}_3, U_{3l}^h\boldsymbol{e}_3)_\Sigma\right)_{kl}, \\
\boldsymbol{A} &= \left(2\mu(D(\boldsymbol{V}_k^h), D(\boldsymbol{V}_l^h))_{\Omega^-\cup\Omega^+}\right)_{kl}, & \boldsymbol{B} &= \left((P_k^h, \nabla\cdot\boldsymbol{V}_l^h)_{\Omega^-\cup\Omega^+}\right)_{kl}, \\
\boldsymbol{P}_A &= \left((\underline{\boldsymbol{A}}^{\hom} D_{\bar{x}}(\bar{\boldsymbol{U}}_l^h), D_{\bar{x}}(\bar{\boldsymbol{U}}_k^h))_\Sigma\right)_{kl}, \\
\boldsymbol{P}_C &= \left((\underline{\boldsymbol{C}}^{\hom}\nabla_{\bar{x}}^2(U_{3\,l}^h), \nabla_{\bar{x}}^2(U_{3\,k}^h))_\Sigma\right)_{kl}, \\
\boldsymbol{P}_{B_1} &= \left((\underline{\boldsymbol{B}}^{\hom}\nabla_{\bar{x}}^2(U_{3\,l}^h), D_{\bar{x}}(\bar{\boldsymbol{U}}_k^h))_\Sigma\right)_{kl}, \\
\boldsymbol{P}_{B_2} &= \left((\underline{\boldsymbol{B}}^{\hom} D_{\bar{x}}(\bar{\boldsymbol{U}}_l^h), \nabla_{\bar{x}}^2(U_{3\,k}^h))_\Sigma\right)_{kl}
\end{aligned}$$

and time-dependent right-hand side $\boldsymbol{L}(t) = (\boldsymbol{F}(t), 0, 0, \boldsymbol{G}_3(t), 0)^T$ with blocks

$$\boldsymbol{F}(t) = \left((\boldsymbol{f}(t), \boldsymbol{V}_k^h)_{\Omega^-\cup\Omega^+}\right)_k, \quad \boldsymbol{G}_3(t) = \left(-(g_3(t), U_{3\,k}^h)_\Sigma\right)_k.$$

Note that in general one has $\boldsymbol{P}_{B_1} \neq \boldsymbol{P}_{B_2}^T$.

For the stationary case, the fully discrete formulation consists of the two linear systems

$$\begin{pmatrix} \boldsymbol{A} + \boldsymbol{R}_{VV} & -\boldsymbol{B}^T \\ -\boldsymbol{B} & 0 \end{pmatrix}\begin{pmatrix} \boldsymbol{v}^h \\ p^h \end{pmatrix} = \begin{pmatrix} \boldsymbol{F} \\ 0 \end{pmatrix}, \quad \begin{pmatrix} \boldsymbol{P}_A & \boldsymbol{P}_{B_1} \\ \boldsymbol{P}_{B_2} & \boldsymbol{P}_C \end{pmatrix}\begin{pmatrix} \bar{\boldsymbol{u}}^h \\ u_3^h \end{pmatrix} = \begin{pmatrix} 0 \\ \boldsymbol{G}_3 + \boldsymbol{R}_{VU}^T\boldsymbol{v}^h \end{pmatrix},$$

which can be solved in sequential order.

For the choice of specific FE spaces, a spatial decomposition of Ω using a regular hexahedral mesh is proposed. The mesh is chosen as Σ-conforming in the sense that

its restriction to the interface Σ is a quadrilateral 2D mesh given by the element facets. A reformulation with a tetrahedral decomposition is straightforward.

In what follows, the hexahedral elements are denoted by $T \in \mathcal{T}^h$, while the facets of Σ are denoted by $F \in \mathcal{F}^h$.

For the velocity variables, the classical $\mathcal{Q}_2/\mathcal{Q}_1$ Taylor–Hood pairing is chosen. Since $\boldsymbol{v}$ is continuous on Σ, while p has a jump discontinuity on Σ, the respective FE spaces read

$$\mathcal{V}^h = \{\boldsymbol{v}^h \in C^0(\Omega)^3 : v_i^h|_T \in \mathcal{Q}_{k+1} \text{ for all } T \in \mathcal{T}^h, i = 1,2,3\} \cap \mathcal{V},$$
$$\mathcal{P}^h = \{p^h : p^h|_{\Omega^\pm} \in C^0(\Omega^\pm), p^h|_T \in \mathcal{Q}_k \text{ for all } T \in \mathcal{T}^h\}.$$

The resulting pressure mesh has a fissure on Σ, with each mesh node on Σ being associated with two pressure DOF, respectively. The authors in [16] performed comparative studies for a similar stationary Stokes-Stokes problem with globally continuous pressure space. Unsurprisingly, this choice leads to poor results unless the discretization size is sufficiently small around Σ. Furthermore, for the stationary case, the authors in [16] derived an applicable stabilization approach based on the classical pressure-Poisson method for the unstable $\mathcal{Q}_1/\mathcal{Q}_1$ pairing.

For the plate's in-plane displacement, $\mathcal{Q}_1$ interpolation in 2D is employed. The H^2-conformity of the deflection u_3 requires continuous first-order derivatives of the FE across edges in the mesh, i.e., C^1-elements. For quadrilateral meshes, the employment of BFS elements (see [5, 8]) is proposed, which are bicubic polynomials that are comparatively easy to self-implement.

The corresponding FE spaces are

$$\bar{\mathcal{U}}^h = \{\bar{\boldsymbol{u}}^h \in C^0(\Sigma)^2 : \bar{u}_i^h|_F \in \mathcal{Q}_1 \text{ for all } F \in \mathcal{F}^h, i = 1,2\} \cap \bar{\mathcal{U}},$$
$$\mathcal{U}_3^h = \{u_3^h \in C^1(\Sigma) : u_3^h|_F \in \mathcal{Q}_3 \text{ for all } F \in \mathcal{F}^h\} \cap \mathcal{U}_3.$$

A standard basis of the BFS elements in $\mathbb{R}^n$ is attained from tensor products of classical 1D Hermite splines. On the unit interval $[0,1]$, the latter read

$$\hat{H}_{00}(x) = (2x+1)(x-1)^2, \quad \hat{H}_{10}(x) = x(x-1)^2,$$
$$\hat{H}_{01}(x) = x^2(3-2x), \quad \hat{H}_{11}(x) = x^2(x-1),$$

which generalizes to arbitrary intervals $[x^0, x^1]$ with length $L = x^1 - x^0$ by the affine change of variables

$$H_{00}(x) = \hat{H}_{00}\left(\frac{x-x^0}{L}\right), \quad H_{10}(x) = L\hat{H}_{10}\left(\frac{x-x^0}{L}\right),$$
$$H_{01}(x) = \hat{H}_{01}\left(\frac{x-x^0}{L}\right), \quad H_{11}(x) = L\hat{H}_{11}\left(\frac{x-x^0}{L}\right).$$

A sketch of the 1D splines on the unit interval is shown in Figure 5. The corresponding 1D FE are commonly referred to as *Hermite* elements; see [9].

The BFS basis polynomials are attained by computing tensor products of the Hermite splines. Let $[x_1^0, x_1^1] \times \cdots \times [x_n^0, x_n^1]$ denote an arbitrary cuboid in $\mathbb{R}^n$ with edge lengths $L_i = x_i^1 - x_i^0$. One defines the 4^n basis polynomials as

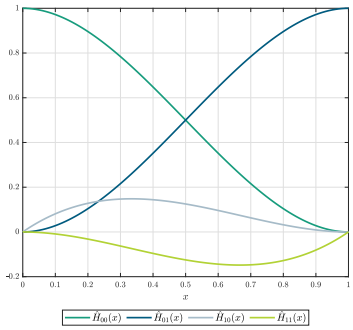

FIG. 5. *Hermite splines on unit interval.*

$$B_{\boldsymbol{\alpha},\boldsymbol{\beta}}(x) := \prod_{i=1}^{n} L_i^{\alpha_i} \hat{H}_{\alpha_i\beta_i}\left(\frac{x_i - x_i^0}{L_i}\right), \quad \boldsymbol{\alpha},\boldsymbol{\beta} \in \{0,1\}^n,$$

which for the unit cube $[0,1]^n$ results in the reference functions

$$\hat{B}_{\boldsymbol{\alpha},\boldsymbol{\beta}}(x_1,x_2) := \prod_{i=1}^{n} \hat{H}_{\alpha_i\beta_i}(x_i), \quad \boldsymbol{\alpha},\boldsymbol{\beta} \in \{0,1\}^n.$$

One can derive that the interpolant of $w \in C^1([x_1^0,x_1^1]\times\cdots\times[x_n^0,x_n^1])$ by the BFS polynomials reads

$$\Pi_{\mathrm{BFS}}[w](x) = \sum_{\boldsymbol{\alpha},\boldsymbol{\beta}\in\{0,1\}^n} \partial_{x_1}^{\alpha_1}\cdots\partial_{x_n}^{\alpha_n} w(x_1^{\beta_1},\ldots,x_n^{\beta_n}) B_{\boldsymbol{\alpha},\boldsymbol{\beta}}(x).$$

Therefore, one can associate the 4^n nodal DOF $\partial_{x_1}^{\alpha_1}\cdots\partial_{x_n}^{\alpha_n} w(x_1^{\beta_1},\ldots,x_n^{\beta_n})$ per element.

Hence, for the specific choice of $n = 2$, for each mesh node on Σ, one attains the deflection's value, the value of its two first-order derivatives, as well as the value of the mixed second-order derivative. It is noted that for unstable lattice structures (see [22]), the mixed derivatives are unknown. For these types of structures, the recent work [15] offers even more effective bicubic interpolation, avoiding mixed derivatives.

In Figure 6, 4 of the 16 derived shape functions for $n = 2$ are plotted that are associated with the point $(1,0)$. The remaining functions are of a similar nature.

As an alternative to the H^2-conforming elements, penalty methods such as the continuous-discontinuous Galerkin approach [14] are applicable. The interested reader is referred, e.g., to [11] for a recent application in the FSI context for the simulation of thin floating structures, modeled by Kirchhoff plates.

As a summary, the resulting amount of DOF per respective element for the chosen spatial discretization is listed in Table 1.

4. Simulation results.

4.1. Qualitative description of stiffness tensors. In the following section, the influence of entries in the homogenized stiffness tensors on the overall behavior of the homogenized filter structure under different loading scenarios is described

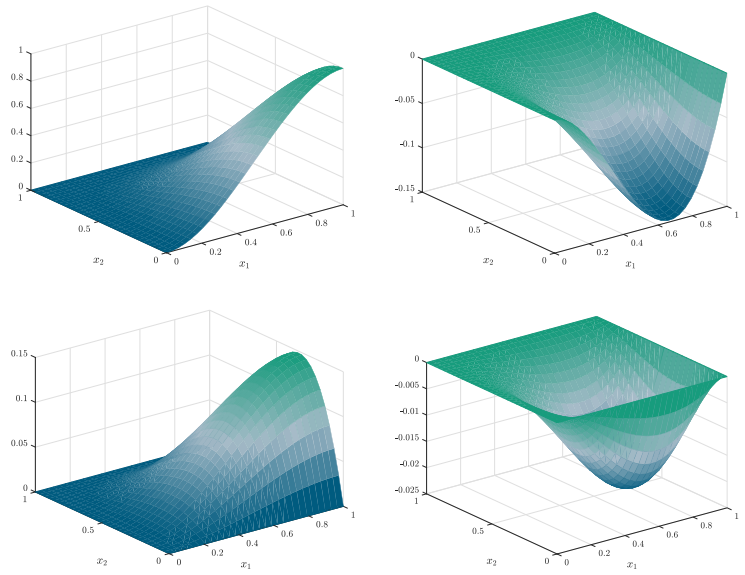

FIG. 6. *The four BFS shape functions* $\hat{B}_{(0,0),(1,0)}, \hat{B}_{(1,0),(1,0)}, \hat{B}_{(0,1),(1,0)}, \hat{B}_{(1,1),(1,0)}$ *on the unit square.*

TABLE 1
Summary of employed FE.

Function	$\boldsymbol{v}^h$	p^h	$\bar{\boldsymbol{u}}^h$	u_3^h
FE type	$\mathcal{Q}_2$	$\mathcal{Q}_1$	$\mathcal{Q}_1$	BFS
DOF per element	27	8	4	16

qualitatively. The discussion enables the quantitative analysis of the entries in the subsequent section.

Remark 4.1. With the knowledge about symmetry of the homogenized stiffness tensors $\underline{\boldsymbol{A}}^{\text{hom}}, \underline{\boldsymbol{C}}^{\text{hom}}$ from Lemma 2.4, one deduces that there are at most six independent entries per tensor, which are represented in a symmetric 3×3 matrix of the form

$$\underline{\boldsymbol{A}}^{\text{hom}} = \begin{pmatrix} a_{1111}^{\text{hom}} & a_{1122}^{\text{hom}} & a_{1112}^{\text{hom}} \\ * & a_{2222}^{\text{hom}} & a_{2212}^{\text{hom}} \\ * & * & a_{1212}^{\text{hom}} \end{pmatrix}, \quad \underline{\boldsymbol{C}}^{\text{hom}} = \begin{pmatrix} c_{1111}^{\text{hom}} & c_{1122}^{\text{hom}} & c_{1112}^{\text{hom}} \\ * & c_{2222}^{\text{hom}} & c_{2212}^{\text{hom}} \\ * & * & c_{1212}^{\text{hom}} \end{pmatrix}.$$

The reduced symmetry of the coupling stiffness tensor enables a representation of the form

$$\underline{\boldsymbol{B}}^{\text{hom}} = \begin{pmatrix} b_{1111}^{\text{hom}} & b_{1122}^{\text{hom}} & b_{1112}^{\text{hom}} \\ b_{2211}^{\text{hom}} & b_{2222}^{\text{hom}} & b_{2212}^{\text{hom}} \\ b_{1211}^{\text{hom}} & b_{1222}^{\text{hom}} & b_{1212}^{\text{hom}} \end{pmatrix}.$$

The qualitative description starts with a result from [42] that describes the effective properties of orthotropic plates.

LEMMA 4.2. *Assume that the microscopic structure is given by an orthotropic* 3*D plate with Young's moduli* E_1, E_2*, Poisson's ratios* ν_{12}, ν_{21}*, shear modulus* G*, as well as a constant thickness denoted by* δ*. Then the homogenized tensors are given by*

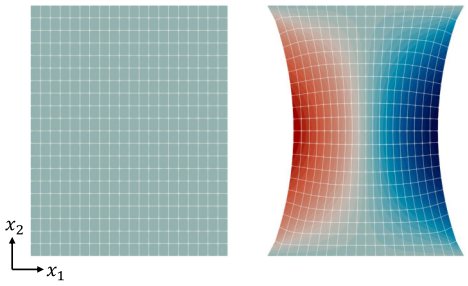

FIG. 7. *Displacement of homogenized textile under applied tension in the x_2-direction for a zero (left) and a large, nonzero value of a^{hom}_{2211} (right). Free lateral boundary left and right. Colors indicate displacement in the x_1-direction.*

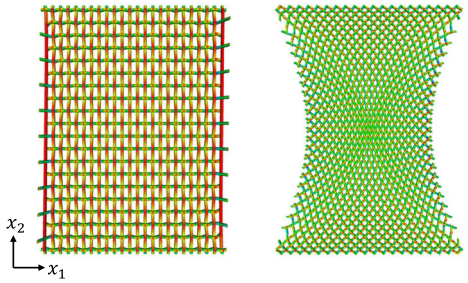

FIG. 8. *Comparison of transverse contraction under applied tension in x_2-direction in microscopic simulation. Yarn orientation along the Cartesian coordinates (left) and rotated by 45° (right). Free lateral boundary left and right with colors indicating local stresses.*

$$\underline{\boldsymbol{A}}^{hom} = \frac{\delta}{12(1-\nu_{12}\nu_{21})} \begin{pmatrix} E_1 & \nu_{21}E_1 & 0 \\ * & E_2 & 0 \\ * & * & 12(1-\nu_{12}\nu_{21})G \end{pmatrix},$$

$$\underline{\boldsymbol{C}}^{hom} = \frac{\delta^3}{12(1-\nu_{12}\nu_{21})} \begin{pmatrix} E_1 & \nu_{21}E_1 & 0 \\ * & E_2 & 0 \\ * & * & (1-\nu_{12}\nu_{21})G \end{pmatrix}$$

and $\underline{\boldsymbol{B}}^{hom}$ vanishes.

Remark 4.3. It is noted that due to the orthotropy constraint $\frac{E_2}{E_1} = \frac{\nu_{21}}{\nu_{12}}$, one can alternatively write $\nu_{12}E_2$ in the second entries in $\underline{\boldsymbol{A}}^{\text{hom}}, \underline{\boldsymbol{C}}^{\text{hom}}$ in Lemma 4.2, respectively.

The relations in Lemma 4.2, as well as the appearance of the respective entries in the governing macroscopic plate equations, provide an intuitive understanding of $\underline{\boldsymbol{A}}^{\text{hom}}$ and $\underline{\boldsymbol{C}}^{\text{hom}}$. The entries a^{hom}_{1111} and a^{hom}_{2222} determine the resistance to applied normal tensional loads, while the ratios $\frac{a^{\text{hom}}_{1122}}{a^{\text{hom}}_{1111}}$ and $\frac{a^{\text{hom}}_{2211}}{a^{\text{hom}}_{2222}}$ determine the transverse contraction under normal tensional loads.

A simulation scenario exemplarily showing the influence of a^{hom}_{2211} on this Poisson effect is presented in Figure 7 and a corresponding microscopic simulation is shown in Figure 8.

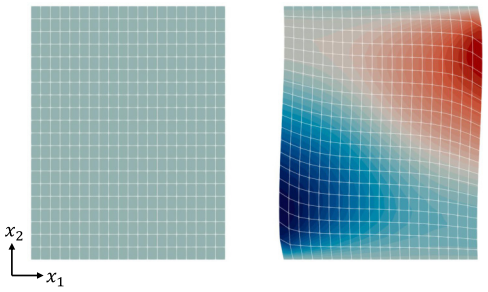

FIG. 9. *Displacement of homogenized textile under applied tension in the x_2-direction for a zero (left) and a large, nonzero value of a^{hom}_{1222} (right). Free lateral boundary left and right. Colors indicate displacement in x_1-direction.*

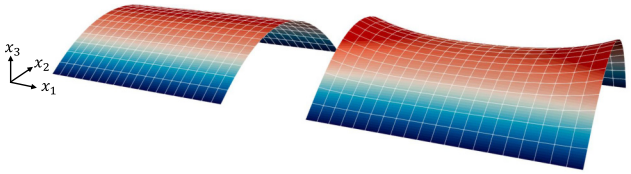

FIG. 10. *Displacement of homogenized textile under applied bending along the x_2-direction for zero (left) and a large, nonzero value of c^{hom}_{2211} (right). Free lateral boundary left and right. Colors indicate deflection.*

The tensor entry a^{hom}_{1212} gives a measure of resistance to shearing loads, while the remaining off-diagonal entries $a^{\text{hom}}_{1112}, a^{\text{hom}}_{2212}$ introduce a coupling of normal tension and shearing of the textile. An illustrative example is presented in Figure 9.

The off-diagonal entries of $\underline{\boldsymbol{A}}^{\text{hom}}$ may as well be negative. In case of a^{hom}_{1122} being negative, one speaks of *auxetic structures,* that expand in the transverse direction under normal tensional loads. Changing the sign of a^{hom}_{1222} in Figure 9 causes a mirroring of the displacement along the x_2-axis.

Similar effective outer-plane bending properties can be formulated for the entries of $\underline{\boldsymbol{C}}^{\text{hom}}$. Qualitatively, the values c^{hom}_{1111} and c^{hom}_{2222} determine the stiffness w.r.t. normal bending loads, commonly referred to as *flexural rigidity.*

The ratios $\frac{c^{\text{hom}}_{1122}}{c^{\text{hom}}_{1111}}$ and $\frac{c^{\text{hom}}_{2211}}{c^{\text{hom}}_{2222}}$ determine the tendency of transverse bending under normal bending loads, effectively leading to saddle-point formations, i.e., hyperbolic paraboloids.

The effect is depicted in Figure 10 and for a microscopic simulation in Figure 11.

Further, the entry c^{hom}_{1212} is a measure for torsional stiffness, while the remaining off-diagonal entries $c^{\text{hom}}_{1112}, c^{\text{hom}}_{2212}$ introduce an additional coupling between bending and torsion. The coupling effect is demonstrated in Figure 12.

Similar to $\underline{\boldsymbol{A}}^{\text{hom}}$, changing the sign of the off-diagonal entries in $\underline{\boldsymbol{C}}^{\text{hom}}$ results in the inverted transverse bending for c^{hom}_{2211}, as well as a mirroring of the displacement in Figure 12 for c^{hom}_{2212}.

From the governing plate equations, one can derive that each entry of $\underline{\boldsymbol{B}}^{\text{hom}}$ couples an in-plane strain to a bending moment and vice versa. For illustration, the influence of b^{hom}_{2211} and b^{hom}_{2222} is presented: Consider the case of tension applied in the x_2-direction which translates to the displacement only in the in-plane direction for the case $b^{\text{hom}}_{2211} = b^{\text{hom}}_{2222} = 0$. On the other hand, additional coupling with the bending along the x_1-direction is observed in case of a nonzero value b^{hom}_{2211}, leading

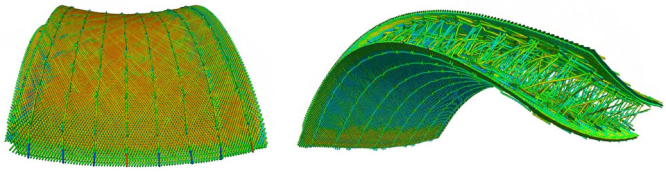

FIG. 11. *Example for a hyperbolic paraboloid forming under bending of a spacer fabric due to nonzero* c^{hom}_{2212}. *Colors indicate local stresses.*

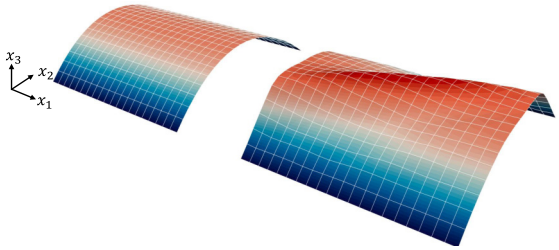

FIG. 12. *Displacement of homogenized textile under applied bending along the* x_2*-direction for zero (left) and a large, nonzero value of* c^{hom}_{2212} *(right). Free lateral boundary left and right. Colors indicate deflection.*

to a buckling or wrinkling effect. If b^{hom}_{2222} is nonzero, the applied strain translates into an additional bending along the x_2-direction. All displacements are presented in Figure 13.

A microscopic simulation with a similar behavior under applied tension in the x_2-direction is shown in Figure 14.

4.2. Quantitative description of stiffness tensors. Using the derived qualitative descriptions from the previous section, attained quantitative simulation results are discussed in the following examples. Here and in the following, the results are attained for a woven structure with parameterization depicted in Figure 15, and values corresponding to a filter made out of PET are listed in Table 2. The contact matrix is chosen as in Example 2.2 with γ_{friction} chosen as 2×10^{-1}. This comparatively high value is based on qualitative comparison of shearing simulations with the real-life filter behavior.

Utilizing the numerical methods of the previous sections, the following homogenized tensors are attained with symmetry up to machine precision:

$$\underline{\boldsymbol{A}}^{\text{hom}} = \begin{pmatrix} 4.898 \times 10^5 & 2.881 \times 10^2 & -9.978 \times 10^{-1} \\ * & 4.898 \times 10^5 & -9.978 \times 10^{-1} \\ * & * & 3.258 \times 10^4 \end{pmatrix} \text{ N m}^{-1},$$

$$\underline{\boldsymbol{B}}^{\text{hom}} = \begin{pmatrix} 1.105 \times 10^{-16} & 2.284 \times 10^{-16} & 1.613 \times 10^{-15} \\ 2.224 \times 10^{-17} & -3.845 \times 10^{-16} & -1.631 \times 10^{-15} \\ 7.391 \times 10^{-17} & -2.481 \times 10^{-17} & 4.473 \times 10^{-17} \end{pmatrix} \text{ N},$$

$$\underline{\boldsymbol{C}}^{\text{hom}} = \begin{pmatrix} 3.707 \times 10^{-4} & -1.004 \times 10^{-8} & -8.268 \times 10^{-9} \\ * & 3.707 \times 10^{-4} & -8.268 \times 10^{-9} \\ * & * & 1.296 \times 10^{-4} \end{pmatrix} \text{ N m}.$$

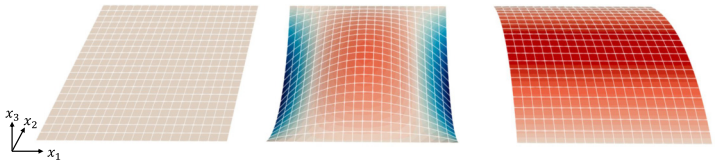

FIG. 13. *Displacement of homogenized textile under tension in the x_2-direction for zero (left) and a large, nonzero value of b^{hom}_{2211} (center), as well as b^{hom}_{2222} (right). Free lateral boundary left and right. Colors indicate deflection.*

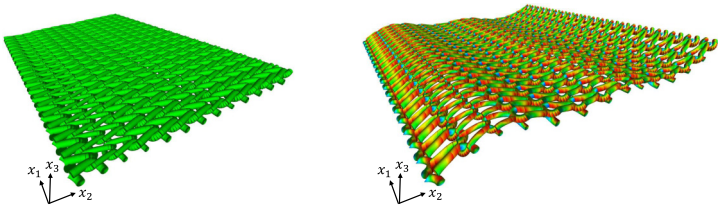

FIG. 14. *Bending along x_2-direction under applied tension in the x_2-direction of a weft-knitted filter with alternating yarn material properties in the x_2-direction. Initial filter (left) and displaced textile (right). Periodic boundary conditions at the lateral boundary. Colors indicate local stresses.*

Qualitatively, these tensor entries are reasonable: The additional symmetry

$$a^{\mathrm{hom}}_{1111} = a^{\mathrm{hom}}_{2222}, \quad a^{\mathrm{hom}}_{1112} = a^{\mathrm{hom}}_{2212},$$
$$c^{\mathrm{hom}}_{1111} = c^{\mathrm{hom}}_{2222}, \quad c^{\mathrm{hom}}_{1112} = c^{\mathrm{hom}}_{2212}$$

is observed, which stems from the rotational symmetry of the weave unit itself. Moreover, the $\underline{\boldsymbol{B}}^{\mathrm{hom}}$ entries are vanishing up to machine precision in accordance to Proposition 3.1.

As to be expected for wovens, the in-plane stiffness is dominant with the largest entries given by the tensional stiffness a^{hom}_{iiii}. The shearing resistance is significantly lower. The entry a^{hom}_{1122} is small, resulting in an effective Poisson's ratio close to zero.

By doubling the yarn distance Δ_1 with remaining parameters being kept the same, one attains

$$\underline{\boldsymbol{A}}^{\mathrm{hom}} = \begin{pmatrix} 2.448 \times 10^5 & 1.407 \times 10^2 & -1.161 \times 10^0 \\ * & 4.900 \times 10^5 & 3.586 \times 10^{-1} \\ * & * & 1.090 \times 10^4 \end{pmatrix} \text{ N m}^{-1},$$

$$\underline{\boldsymbol{B}}^{\mathrm{hom}} = \begin{pmatrix} 4.512 \times 10^{-17} & -6.467 \times 10^{-16} & 5.309 \times 10^{-16} \\ 8.081 \times 10^{-18} & 2.281 \times 10^{-16} & -2.705 \times 10^{-16} \\ 3.511 \times 10^{-17} & 3.285 \times 10^{-18} & 7.555 \times 10^{-18} \end{pmatrix} \text{ N},$$

$$\underline{\boldsymbol{C}}^{\mathrm{hom}} = \begin{pmatrix} 1.853 \times 10^{-4} & -4.767 \times 10^{-9} & -1.575 \times 10^{-9} \\ * & 3.707 \times 10^{-4} & -6.919 \times 10^{-9} \\ * & * & 9.720 \times 10^{-5} \end{pmatrix} \text{ N m}.$$

As to be expected, due to the halved yarn density in the x_1-direction, the overall stiffness for tensional and bending loads in the x_1-direction is reduced by roughly 50%, while the stiffness in the x_2-direction is only slightly affected.

In the following plots, further sensitivities are investigated. The focus is laid on the dominant entries of the tensors $\underline{\boldsymbol{A}}^{\mathrm{hom}}$ and $\underline{\boldsymbol{C}}^{\mathrm{hom}}$, respectively. In Figure 16, the influence of varying yarn diameters is presented. For this purpose, the diameters d_1, d_2

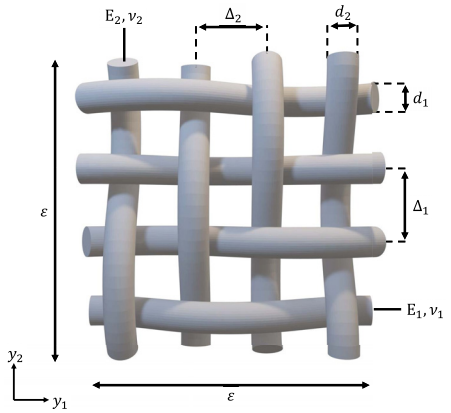

FIG. 15. *Illustration of geometric and elastic parameters for the periodic unit of a twill woven filter.*

TABLE 2
Parameterization of twill woven filter.

Parameter	Unit	Value
ρ_s	g cm^{-3}	1.375
$E_1 = E_2$	GPa	2.95
$\nu_1 = \nu_2$	1	0.43
$\Delta_1 = \Delta_2$	μm	260
$d_1 = d_2$	μm	110
ε	μm	1040

are kept the same on the left-hand-side plots, while only d_2 is varied on the right-hand-side plots. An expected general monotonic dependency on the increasing structure volume density is observed for the first case, while the behavior for the second case is already nontrivial and a quantitative estimate in terms of design parameters proves to be involved even for this relatively simple example.

In Figure 17, the sensitivity on the Young's modulus of the yarn material is shown. As with the diameters, both moduli E_1, E_2 are parameterized the same on the left-hand side, while only E_2 is varied on the right-hand side. Intuitively, the dependence for the first case is almost perfectly linear for both extensional and bending stiffness, while nonlinear dependence arises for the shearing/torsion and off-diagonal entries in the second case.

Last, in Figure 18, the influence of a changing contact parameter γ_{friction} is displayed. Intuitively, the only effected entry of this parameter is the shearing resistance a^{hom}_{1212}. It is observed that the latter is monotonically dependent on the friction, while the remaining tensor entries remain constant. In particular, the bending stiffness is not influenced by the parameter. The small decrease of a^{hom}_{1122} is unexplained at the moment. Moreover, it is observed that a^{hom}_{1212} reaches a steady-state after the threshold of $\gamma_{\text{friction}} \approx 1 \times 10^{-1}$. This regime corresponds to the case of fully glued yarns in which rotation at contact points is prohibited. This locking effect can also be qualitatively observed in the respective perturbated cell solutions; see Figure 19.

As a final example, a filter sample with a nonvanishing coupling stiffness tensor $\underline{\boldsymbol{B}}^{\text{hom}}$ is constructed. First, a 3x3 grid is constructed by repeating the periodic unit of Figure 15 three times in each direction, respectively. Afterward, the yarn diameter

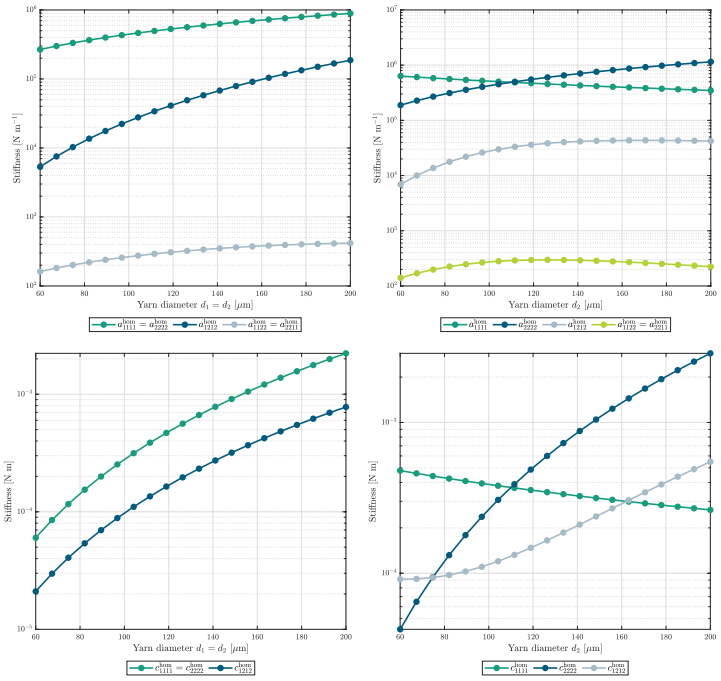

FIG. 16. *Sensitivity of* $\underline{\boldsymbol{A}}^{hom}$ *(top) and* $\underline{\boldsymbol{C}}^{hom}$ *(bottom) to varying yarn diameters.*

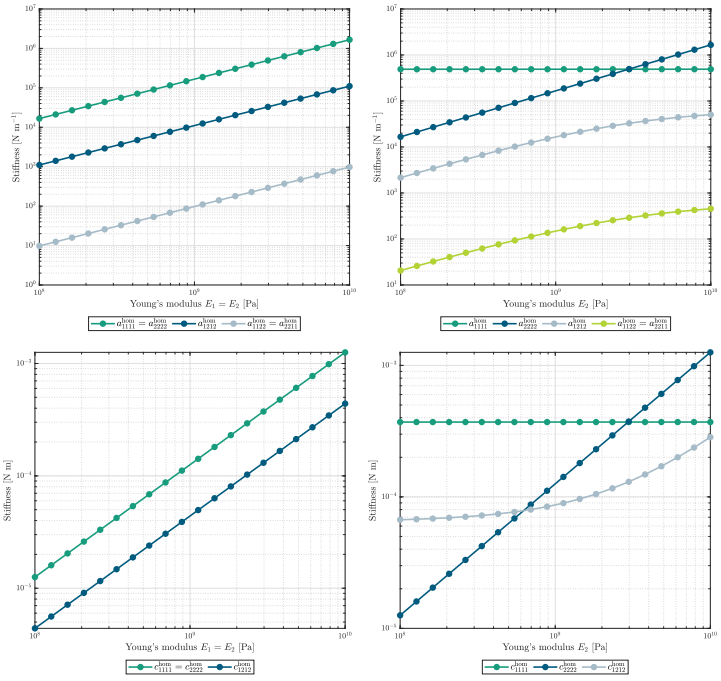

FIG. 17. *Sensitivity of* $\underline{\boldsymbol{A}}^{hom}$ *(bottom) and* $\underline{\boldsymbol{C}}^{hom}$ *(top) to varying Young's moduli of the yarn material.*

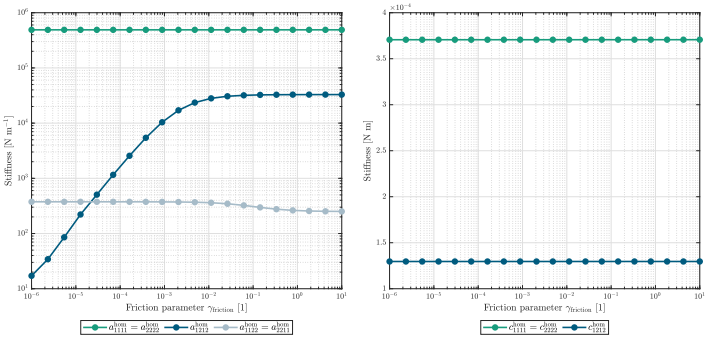

FIG. 18. *Sensitivity of* $\underline{\boldsymbol{A}}^{hom}$ *(left) and* $\underline{\boldsymbol{C}}^{hom}$ *(right) to varying friction parameter.*

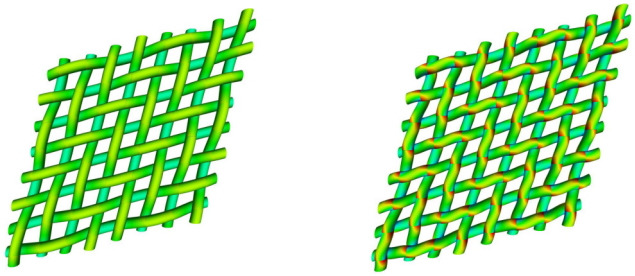

FIG. 19. *Qualitative comparison of perturbated shearing cell solutions* $\boldsymbol{m}_{12}^{M}$ *for a small (left) and a large (right) friction coefficient. Colors indicate local stresses. The periodic unit was repeated two times in each in-plane direction for visualization purposes.*

d_1 is varied only for yarns in the second row of the grid; see Figure 20. Thereby, the asymmetry of the periodic unit can be controlled.

For a value of $d_1 = 200\,\mu$m, one exemplarily attains

$$\underline{\boldsymbol{A}}^{\text{hom}} = \begin{pmatrix} 5.541 \times 10^5 & 8.308 \times 10^2 & -1.818 \times 10^0 \\ * & 4.737 \times 10^5 & 2.038 \times 10^{-1} \\ * & * & 4.134 \times 10^4 \end{pmatrix} \text{ N m}^{-1},$$

$$\underline{\boldsymbol{B}}^{\text{hom}} = \begin{pmatrix} 5.388 \times 10^{-2} & 3.098 \times 10^{-5} & -6.733 \times 10^{-7} \\ 3.006 \times 10^{-5} & 5.388 \times 10^{-2} & -2.273 \times 10^{-6} \\ -3.582 \times 10^{-7} & 7.436 \times 10^{-8} & 4.226 \times 10^{-3} \end{pmatrix} \text{ N},$$

$$\underline{\boldsymbol{C}}^{\text{hom}} = \begin{pmatrix} 4.686 \times 10^{-4} & -3.628 \times 10^{-9} & -4.755 \times 10^{-9} \\ * & 3.878 \times 10^{-4} & -7.670 \times 10^{-9} \\ * & * & 1.509 \times 10^{-4} \end{pmatrix} \text{ N m}.$$

The influence of the choice of d_1 on the entries of $\underline{\boldsymbol{B}}^{\text{hom}}$ is investigated in Figure 21, restricted to the dominant diagonal entries, as well as the entries $b^{\text{hom}}_{1122}, b^{\text{hom}}_{2211}$. For all entries, a minimal value of 0 (up to machine precision) is observed for the fully symmetric case $d_1 = 110\,\mu$m as expected. Even for small deviations around this value, the coupling stiffness tensor attains noticeably larger values. Moreover, the attained curves are nonsymmetric w.r.t. the axis $d_1 = 110\,\mu$m with, e.g., the values $b^{\text{hom}}_{1111}, b^{\text{hom}}_{2222}$ being very close to each other for larger d_1, while there is a clear difference for smaller d_1. Nevertheless, a general monotonic dependence of the entries on the deviation from the fully symmetric case can be observed at least for the investigated parameter range.

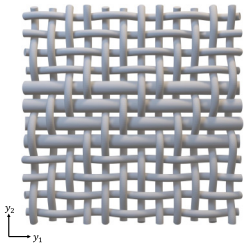

FIG. 20. *Construction of asymmetric filter sample.*

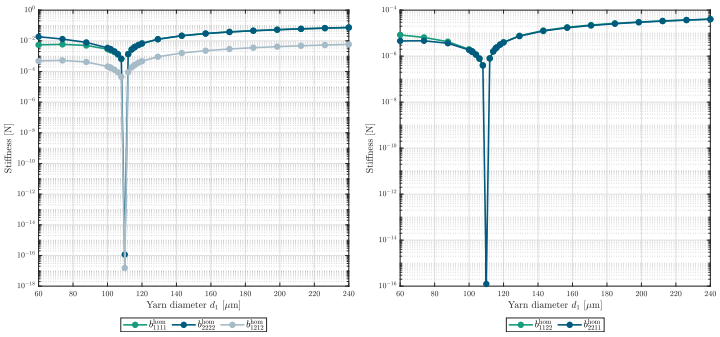

FIG. 21. *Entries of* $\underline{\boldsymbol{B}}^{hom}$ *for the asymmetric filter sample as functions of the yarn diameter* d_1.

4.3. FSI simulations. For the upcoming FSI simulations, the parameters listed in Table 3 are utilized. The microscopic filter structure is chosen as in the previous subsection. The computed permeability tensor for this structure reads

$$\boldsymbol{K} = \begin{pmatrix} 4.93 \times 10^{-8} & -1.14 \times 10^{-10} & -5.05 \times 10^{-14} \\ * & 4.93 \times 10^{-8} & 2.70 \times 10^{-15} \\ * & * & 5.01 \times 10^{-10} \end{pmatrix} \mathrm{m}^2.$$

As a first example, a steady-state solution for the parabolic profile

$$\boldsymbol{v}^{\mathrm{in}}(\bar{x}) = v^{\max} \frac{16}{L_1^2 L_2^2} x_1(L_1 - x_1) x_2(L_2 - x_2) \boldsymbol{e}_3$$

on the inflow boundary is considered, where $v^{\max}$ is chosen as $1 \times 10^2\,\mathrm{mm\,s^{-1}}$. The resulting flow profiles in the respective subdomains $\Omega^{\pm}$ are depicted in Figure 22. Far from the interface region, the velocity profile is parabolic. Close to the interface, it becomes almost constant and normal to Σ. This observation is in accordance with the behavior of flow through rigid Stokes-sieves theoretically proven in and numerically investigated, e.g., in [13, 16]. Individual velocity components are illustrated in Figure 23. The fluid pressure in each subdomain is almost constant with a noticeable jump of 20 Pa at the interface.

To illustrate the flow-induced deflection profile on Σ and its dependence on the filter parameterization on the micro scale, the yarn diameter d_2 is varied as in Figure 16, while the diameter d_1 remains constant. The attained profiles are shown in Figure 24. Note that due to the vanishing coupling stiffness tensor, the in-plane displacements are zero.

TABLE 3
Values of phyiscal parameters in macroscopic FSI simulations.

Parameter	Value	Unit
ρ_f	0.997	g cm^{-3}
μ	1.0016	mPa s
$L_1 = L_2$	1×10^2	mm
L_3	2×10^2	mm

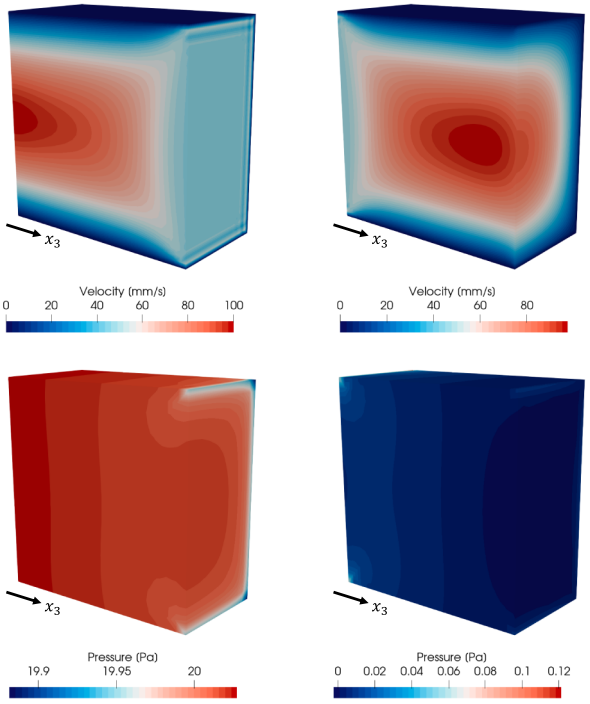

FIG. 22. *Fluid velocity and pressure in cross-sections of individual subdomains* Ω^- *(left) and* Ω^+ *(right).*

In accordance to the observed change from a dominating entry c^{hom}_{1111} to a dominating entry c^{hom}_{2222} in Figure 16, a morphing from a vertically to a horizontally oriented paraboloid is attained for increasing d_2.

Since the yarn diameter not only influences the filter's stiffness, but also monotonically decreases its permeability, the absolute deflection values are actually increasing for an increased yarn diameter. To further investigate the counteracting effect of increasing stiffness versus decreasing permeability, the maximal flow-induced deflections for varying design parameters are depicted in Figure 25. Especially the variation of the yarn diameters results in nontrivial curves that would have not been predictable without the simulation.

To investigate the influence of the coupling stiffness tensor, an FSI simulation for the same setup but with the microstructure in Figure 20 is performed. The attained nonvanishing in-plane displacement $\bar{\boldsymbol{u}}$ is presented in Figure 26. As can be seen, the value of both components u_1, u_2 is significantly smaller than the deflection. Moreover, the absolute value of displacement in the x_1-direction is roughly half of

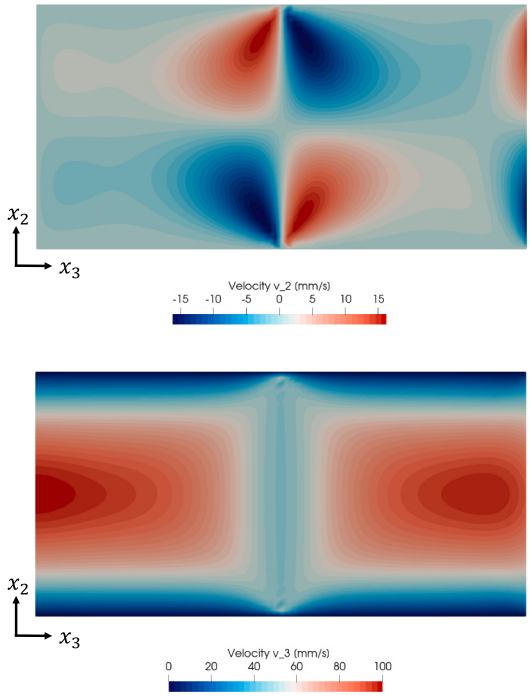

FIG. 23. *Components of the fluid velocity in cross-section of the model domain* Ω.

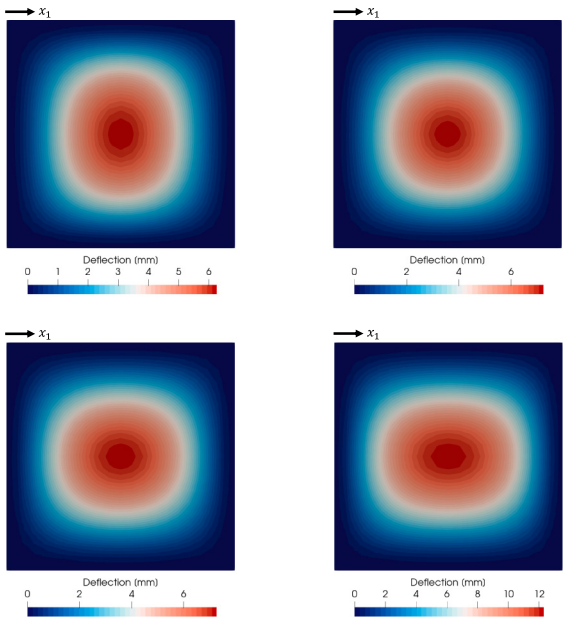

FIG. 24. *Deflection profiles of effective filter for yarn diameters* $d_1 = 110\,\mu$m *and* d_2 *chosen as* 70, 110, 160, *and* 200 μm.

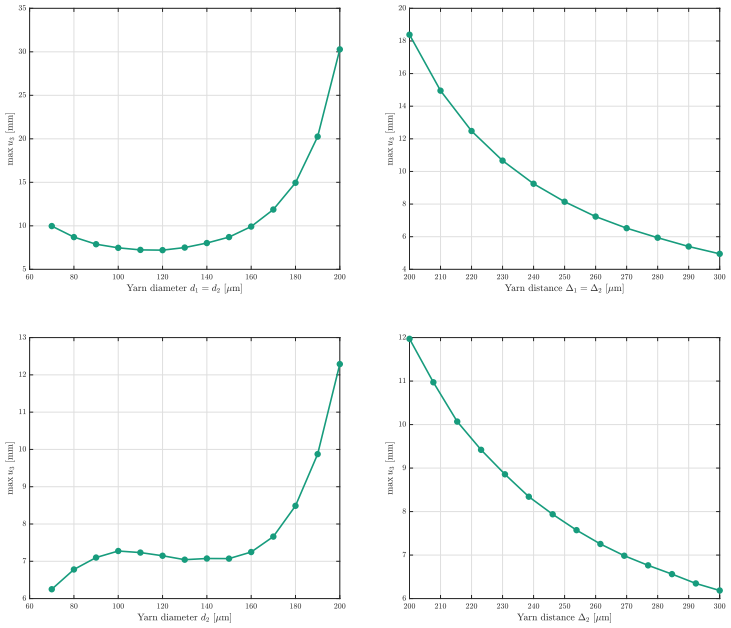

FIG. 25. *Maximal flow-induced deflection of the effective filter for varying design parameters.*

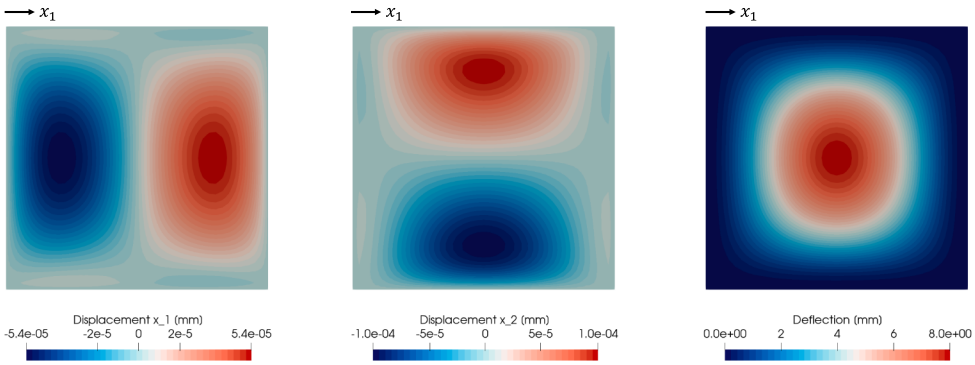

FIG. 26. *Flow-induced in-plane displacement* $\bar{\boldsymbol{u}}$ *and deflection for the asymmetric filter sample.*

the displacement in the x_2-direction, which is intuitive since the extensional stiffness entry a^{hom}_{1111} is larger than the entry a^{hom}_{2222} as a consequence of the added support yarns.

As an example for a nonstationary simulation, the flow through a so-called spacer fabric is investigated. The spacer fabric is modeled as the periodic repetition of the woven sample from Figure 15 in the x_3-direction. The resulting model domain is a sequence of fluid domains, separated by parallel filter fences. A substructure containing 10 of these fences is considered.

The height of the fabric in the x_1-direction is $L_1 = 8 \times 10^1$ mm, while the distance in between two filter fences is 2×10^1 mm. Periodic boundary conditions are applied in the x_2-direction.

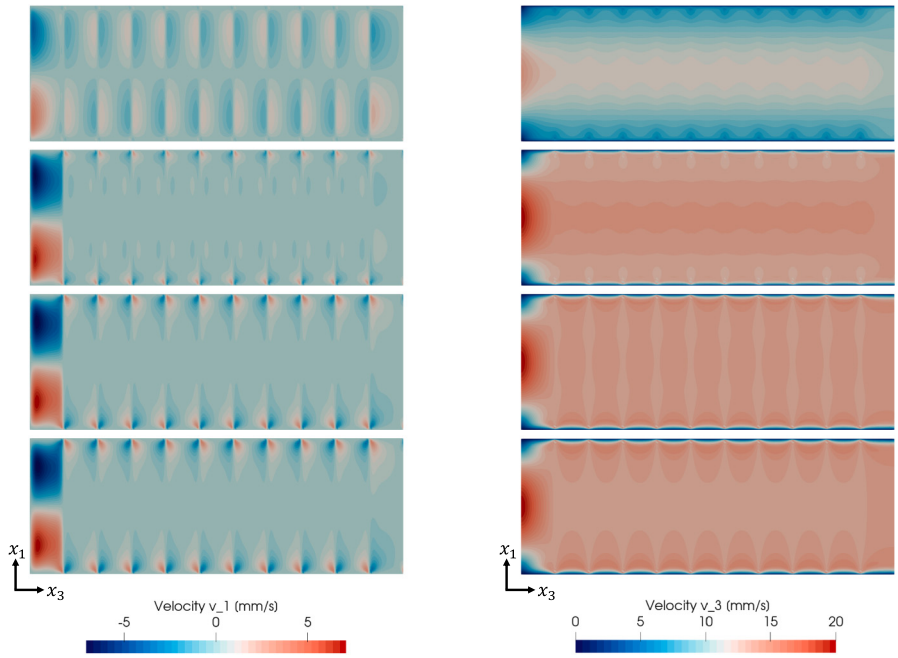

FIG. 27. *Fluid velocity components v_1 and v_3 in cross-section of spacer fabric at time $t = 1, 2, 3, 4$ s.*

The inflow condition at $\{x_3 = 0\}$ is chosen as

$$\boldsymbol{v}^{\text{in}}(t, x_1) = v^{\max}\phi(t)\frac{4}{L_1^2}x_1(L_1 - x_1)\boldsymbol{e}_3, \quad t \in (0, 4),$$

where $\phi(t)$ is the ramp function

$$\phi(t) = \begin{cases} \exp(1)\exp\left(\frac{4}{(t-2)^2-4}\right) & \text{if } 0 \le t < 2, \\ 1 & \text{if } t \ge 2 \end{cases}$$

and $v^{\max} = 2 \times 10^1\,\text{mm}\,\text{s}^{-1}$. The boundary conditions for each fence are slightly modified from a clamped to a simply supported plate.

The attained simulation results at different time steps are presented in Figures 27, 28, and 29. As can be seen, the fluid velocity is identical in each bulk fluid domain apart from the in- and outflow domain. The jump of pressure at each interface is homogeneous as in the stationary case with the same value at each interface. The step-like pressure profile is in accordance with stationary flow simulations performed in a micro resolved spacer fabric in [41]. As a direct consequence, the displacement of each fence is identical. Hence, one may restrict simulations to only two parallel fences.

4.4. Extension with anisotropic model parameters. As discussed at the end of section 2.2, the macroscopic FSI model remains well-posed if one switches from constant macroscopic model parameters to ones which possess L^∞-regularity on Σ. To ensure existence of solutions, one additionally requires coercivity of the permeability tensor almost everywhere on Σ, as well as coercivity of the bilinear form associated to the homogenized stiffness tensors.

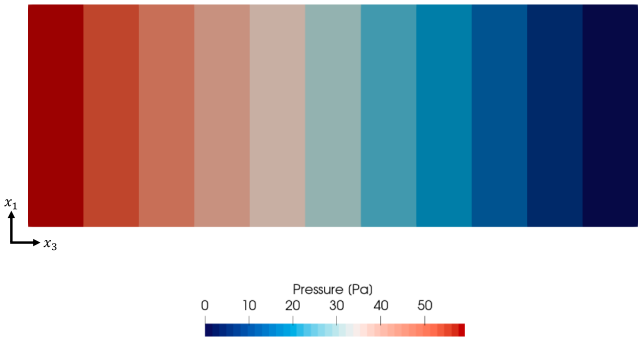

FIG. 28. *Fluid pressure in cross-section of spacer fabric at time* $t = 4$ s.

Such formulations are expected to arise, e.g., if one loosens the periodicity assumption of the microscopic structure to domains with sufficiently *regular* changing structure; see, e.g., [3, section 5 of Chapter 3] for so-called *quasi-periodic structures* in homogenization of linear elasticity.

For these types of structures, one expects the same form of the cell problems and averaging of the cell solution, however, with an additional dependence on the in-plane variable $\bar{x}$, which results in potentially infinitely many cell problems to solve. For numerical methods, one circumvents this difficulty by considering a spatial discretization of Σ, solving the cell problems for each grid-point and performing spatial interpolation afterward.

Application examples in mind cover, e.g., multilayered structures composed of different textile-like filters, as well as patchwork-like fabrics with alternating weaving patterns. For illustration, the flow through a twill woven filter with alternating pattern is considered. One can imagine the structure as a woven filter with equally spaced, parallel, densely woven stripes along the x_2-direction, serving as additional support structures. The distances $\Delta_1 = \Delta_2 = 2.6 \times 10^2\,\mu$m as well as the diameter $d_1 = 1.6 \times 10^2\,\mu$m are chosen. The diameter d_2 is alternating: 24 adjacent yarns have the diameter $4 \times 10^1\,\mu$m, followed by 24 yarns with diameter $1.1 \times 10^2\,\mu$m and again 24 yarns with diameter $4 \times 10^1\,\mu$m. The resulting periodic unit thereby consists of 18 twill weave units and is illustrated in Figure 30. It is periodically repeated 10 times in the x_1-direction and 180 times in the x_2-direction, such that the attained filter is quadratic with edge lengths $L_1 = L_2 = 1.872 \times 10^2$ mm. The channel length is chosen as $L_3 = L_1$.

Since the filter is periodic, one may perform the presented homogenization of the entire unit, analogously to the last example in section 4.2. In the context of quasi-periodic structures, each 4×4 yarn substructure is homogenized to attain piecewise constant homogenized stiffness tensors. The computation of a piecewise constant permeability tensor is performed analogously.

For the FSI simulation, the stationary case with parabolic profile

$$\boldsymbol{v}^{\mathrm{in}}(\bar{x}) = v^{\max} \frac{16}{L_1^2 L_2^2} x_1(L_1 - x_1) x_2(L_2 - x_2) \boldsymbol{e}_3$$

on the inflow boundary is considered, where $v^{\max}$ is chosen as $5 \times 10^1\,\mathrm{mm\,s^{-1}}$.

The attained fluid velocity field, as well as the pressure, are presented in Figures 31 and 32. Due to the smaller permeability in the stripes with larger yarn diameter, the flow mainly passes through the stripes with small yarn diameter. Consequently, on Σ,

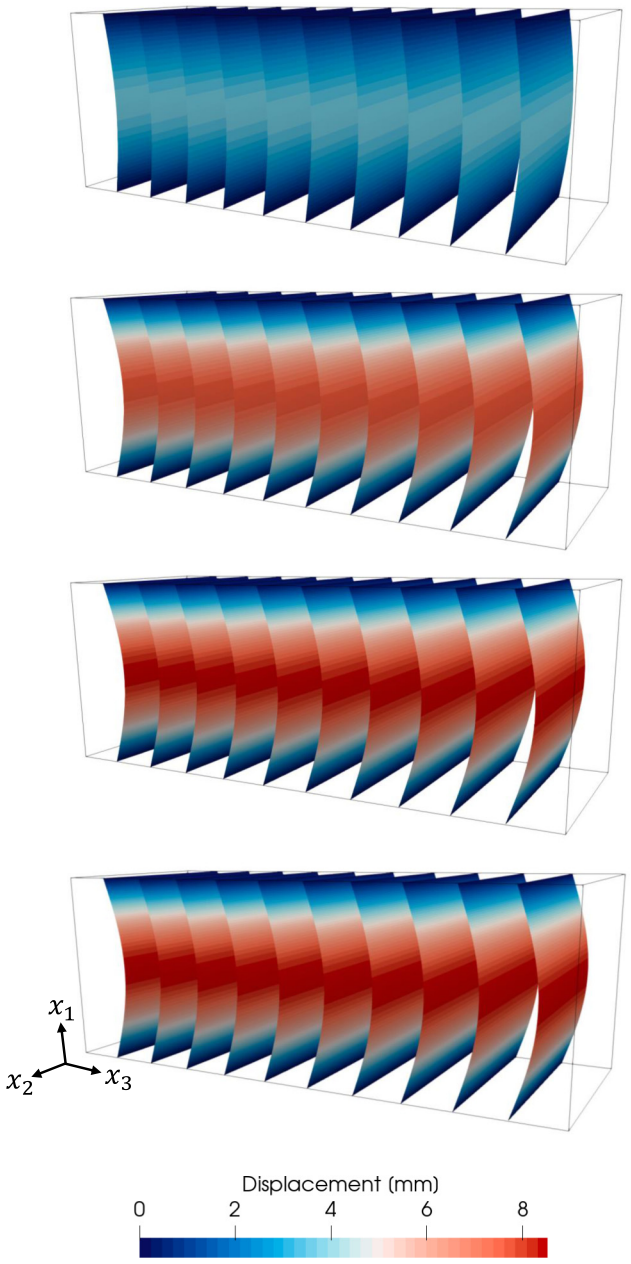

FIG. 29. *Absolute value of structure displacement for spacer fabric at time* $t = 1, 2, 3, 4$ s.

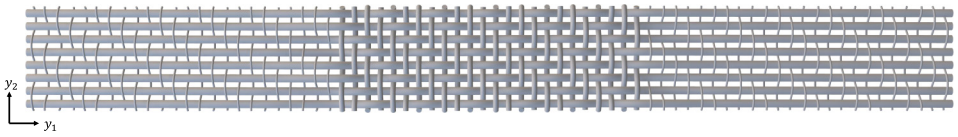

FIG. 30. *Periodic unit of considered filter with alternating yarn diameter* d_2.

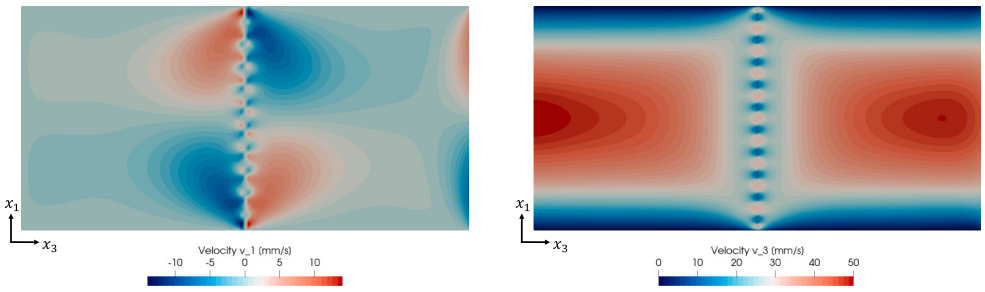

FIG. 31. *Fluid velocity in cross-section of channel for piecewise constant permeability tensor.*

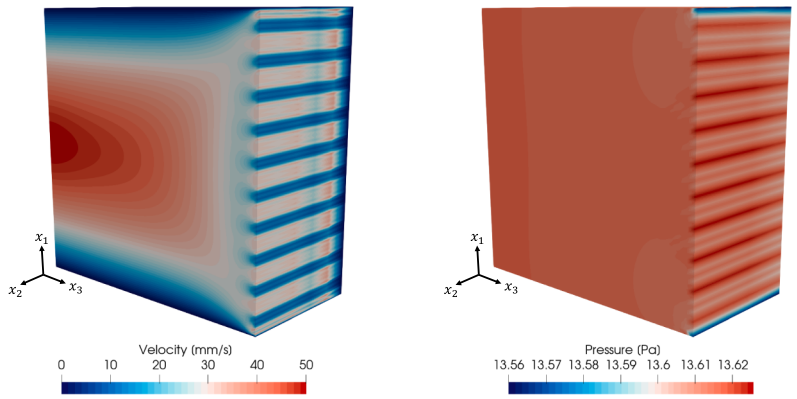

FIG. 32. *Fluid velocity (left) and pressure (right) in cross-section of left subdomain Ω^- for piecewise constant permeability tensor.*

both velocity and pressure are oscillating along the x_1-direction and remain almost constant along the x_2-direction.

For the structure, the flow-induced displacement profile is shown in Figure 33. One attains a terraced profile along the x_1-direction, while the profile is similar to the previous examples along the x_2-direction. Since the jump of fluid stresses is still relatively homogeneous, as can be seen in the small oscillations of the pressure profile in Figure 32, one can deduce that the terrace effect mainly stems from the alternating bending stiffness. The deduction is confirmed by pure structure simulations with constant right-hand-side functions.

5. Conclusions. A complete numerical workflow for the efficient simulation of flow through thin, periodic, flexural filters was presented. The considered multiscale FSI model coupled Stokes flow with a homogenized porous plate, whose effective stiffness tensors and permeability tensor are attained by solving cell solutions on the microresolved periodic unit of the filter.

For the computation of the stiffness tensors, a dimension reduction approach was employed to textile-like filters consisting of individual yarns. The approach allowed the usage of 1D beam FEs to efficiently determine extensional, coupling, and bending stiffness tensors of the structure. The presented method not only is applicable in the FSI context, but is also of interest for general multiscale simulations with textiles and textile-like structures. The computation of the permeability tensor on the micro scale was performed by standard means with a finite volume solver.

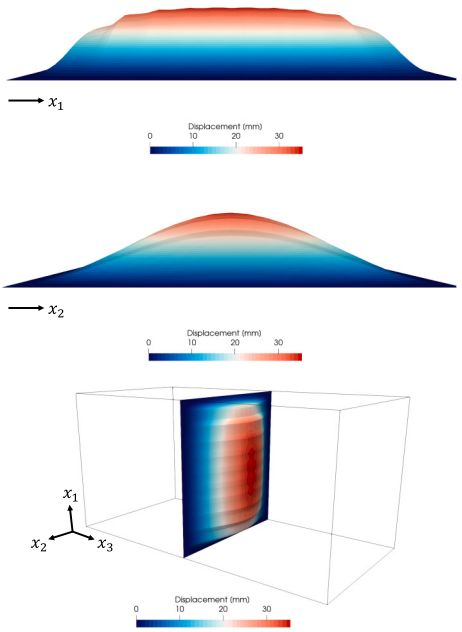

FIG. 33. *Displacement profile for piecewise constant homogenized stiffness tensors.*

A monolithic, conforming FE formulation was presented for the macroscopic FSI system and exemplified for different stationary and nonstationary simulation scenarios. For the fluid variables, the LBB stable Taylor–Hood pairing was chosen. To ensure H^2-conformity of the deflection variable, bicubic Bogner–Fox–Schmit elements were employed.

Concerning the asymptotic analysis, future research should be focused on the rigorous derivation of the proposed permeable interface condition and associated cell problems. Moreover, for application in more general filtration applications, the model should be extended to Navier–Stokes flow to cover higher flow-velocity regimes. For this purpose, the phenomological Darcy interface condition could be generalized, e.g., to a Darcy–Forchheimer-like interface condition. Furthermore, for larger flow-induced filter displacements, a formulation with displacement-dependent domains needs to be derived. Future research may additionally be focused on a generalization with a displacement-dependent permeability tensor, accounting for reduced flow resistance due to larger pore sizes in the displaced filter state.

REFERENCES

[1] G. ALLAIRE, *Homogenization of the Navier-Stokes equations in open sets perforated with tiny holes. II. Noncritical sizes of the holes for a volume distribution and a surface distribution of holes*, Arch. Ration. Mech. Anal., 113 (1990), pp. 261–298, https://doi.org/10.1007/BF00375066.

[2] Y. AMIRAT, O. BODART, G. A. CHECHKIN, AND A. L. PIATNITSKI, *Asymptotics of a spectral-sieve problem*, J. Math. Anal. Appl., 435 (2016), pp. 1652–1671, https://doi.org/10.1016/j.jmaa.2015.11.014.

[3] N. BAKHVALOV AND G. PANASENKO, *Homogenisation: Averaging Processes in Periodic Media*, Kluwer, Dordrecht, Netherlands, 1989.

[4] L. Bociu, S. Canic, B. Muha, and J. T. Webster, *Multilayered poroelasticity interacting with Stokes flow*, SIAM J. Math. Anal., 53 (2021), pp. 6243–6279, https://doi.org/10.1137/20M1382520.
[5] F. K. Bogner, R. L. Fox, and L. A. Schmit, *The generation of interelement compatible stiffness and mass matrices by the use of interpolation formulae*, in Proceedings of the Conference on Matrix Methods in Structural Mechanics, 1965, pp. 397–444.
[6] A. Brillard, *Asymptotic flow of a viscous and incompressible fluid through a plane sieve*, in Progress in Partial Differential Equations: Calculus of Variations, Applications (Pont-à-Mousson, 1991), Pitman Res. Notes Math. Ser. 267, C. Bandle, J. Bemelmans, M. Chipot, M. Grüter, and J. Saint Jean Paulin, eds., Longman, Harlow, UK, 1992, pp. 158–172.
[7] T. Carraro, E. Marušić-Paloka, and A. Mikelić, *Effective pressure boundary condition for the filtration through porous medium via homogenization*, Nonlinear Anal. Real World Appl., 44 (2018), pp. 149–172, https://doi.org/10.1016/j.nonrwa.2018.04.008.
[8] P. G. Ciarlet, *The Finite Element Method for Elliptic Problems*, SIAM, Philadelphia, 2002.
[9] P. G. Ciarlet and P.-A. Raviart, *Interpolation theory over curved elements, with applications to finite element methods*, Comput. Methods Appl. Mech. Engrg., 1 (1972), pp. 217–249, https://doi.org/10.1016/0045-7825(72)90006-0.
[10] D. Cioranescu, A. Damlamian, G. Griso, and D. Onofrei, *The periodic unfolding method for perforated domains and Neumann sieve models* J. Math. Pures Appl., 89 (2008), pp. 248–277.
[11] O. Colomés, F. Verdugo, and I. Akkerman, *A monolithic finite element formulation for the hydroelastic analysis of very large floating structures*, Numer. Methods Eng., 124 (2023), pp. 714–751, https://doi.org/10.1002/nme.7140.
[12] C. Conca, *Étude d'un fluide traversant une paroi perforée.* I. *Comportement limite près de la paroi*, J. Math. Pures Appl. (9), 66 (1987), pp. 1–43.
[13] C. Conca and M. Sepúlveda, *Numerical results in the Stokes sieve problem*, Rev. Internac. Métod. Numér. Cálc. Disen. Ingr., 5 (1989), pp. 435–452.
[14] G. Engel, K. Garikipati, T. Hughes, M. Larson, L. Mazzei, and R. Taylor, *Continuous/discontinuous finite element approximations of fourth-order elliptic problems in structural and continuum mechanics with applications to thin beams and plates, and strain gradient elasticity*, Comput. Methods Appl. Mech. Engrg., 191 (2002), pp. 3669–3750, https://doi.org/10.1016/S0045-7825(02)00286-4.
[15] R. Falconi, G. Griso, and J. Orlik, *Periodic unfolding for lattice structures*, Ric. Mat., (2022), pp. 1–35, https://doi.org/10.1007/s11587-022-00729-x.
[16] M. A. Fernández, J.-F. Gerbeau, and V. Martin, *Numerical simulation of blood flows through a porous interface*, ESAIM Math. Model. Numer. Anal., 42 (2008), pp. 961–990, https://doi.org/10.1051/m2an:2008031.
[17] Fraunhofer Institute for Industrial Mathematics ITWM, *Department of Flow and Material Simulation*, itwm.fraunhofer.de/texmath_en.
[18] M. Gahn, W. Jäger, and M. Neuss-Radu, *Derivation of stokes-plate-equations modeling fluid flow interaction with thin porous elastic layers*, Appl. Anal., 101 (2022), pp. 4319–4348, https://doi.org/10.1080/00036811.2022.2080673.
[19] D. Gómez and M.-E. Pérez-Martínez, *Boundary homogenization with large reaction terms on a strainer-type wall*, Z. Angew. Math. Phys., 73 (2022), 234, https://doi.org/10.1007/s00033-022-01869-8.
[20] G. Griso, *Decompositions of displacements of thin structures*, J. Math. Pures Appl., 89 (2008), pp. 199–223, https://doi.org/10.1016/j.matpur.2007.12.007.
[21] G. Griso, M. Hauck, and J. Orlik, *Asymptotic analysis for periodic perforated shells*, ESAIM Math. Model. Numer. Anal., 55 (2021), pp. 1–36, https://doi.org/10.1051/m2an/2020067.
[22] G. Griso, L. Khilkova, and J. Orlik, *Asymptotic behavior of 3d unstable structures made of beams*, J. Elasticity, 150 (2022), pp. 7–76, https://doi.org/10.1007/s10659-022-09892-6.
[23] G. Griso, L. Khilkova, J. Orlik, and O. Sivak, *Homogenization of perforated elastic structures*, J. Elasticity, 141 (2020), pp. 181–225, https://doi.org/10.1007/s10659-020-09781-w.
[24] G. Griso, J. Orlik, and S. Wackerle, *Asymptotic behavior for textiles*, SIAM J. Math. Anal., 52 (2020), pp. 1639–1689, https://doi.org/10.1137/19M1288693.
[25] G. Griso, J. Orlik, and S. Wackerle, *Asymptotic behavior for textiles in Von-Kármán regime*, J. Math. Pures Appl., 144 (2020), pp. 164–193, https://doi.org/10.1016/j.matpur.2020.10.002.
[26] O. Iliev, D. Iliev, and R. Kirsch, *On computer simulation of fluid-porous structure interaction problems for a class of filtration problems*, in Large-Scale Scientific Computing, I. Lirkov, S. D. Margenov, and J. Waśniewski, eds., Springer, Berlin, 2015, pp. 30–41.

[27] O. Iliev, A. Mikelic, and P. Popov, *Fluid Structure Interaction Problems in Deformable Porous Media: Toward Permeability of Deformable Porous Media*, Technical report 65, Fraunhofer (ITWM), 2004.

[28] W. Jäger, A. Mikelic, and M. Neuss-Radu, *Homogenization limit of a model system for interaction of flow, chemical reaction, and mechanics in cell tissues*, SIAM J. Math. Anal., 43 (2011), pp. 1390–1435, https://doi.org/10.1137/100808393.

[29] R. Kirsch, J. Köbler, V. Puderbach, S. Antonyuk, N. Henkelmann, and M. Weirich, *Flow-induced deformation of nonwoven filter media: Experiments, modeling and simulation*, in Proceedings of FILTECH 2023.

[30] M. Krier and J. Orlik, *Solvability of a fluid-structure interaction problem with semigroup theory*, AIMS Math., 8 (2023), pp. 29490–29516, https://doi.org/10.3934/math.20231510.

[31] G. Liu and S. Quek, *The Finite Element Method*, 2nd ed., Butterworth-Heinemann, Oxford, UK, 2014.

[32] A. Marciniak-Czochra and A. Mikelić, *A rigorous derivation of the equations for the clamped Biot-Kirchhoff-Love poroelastic plate*, Arch. Ration. Mech. Anal., 215 (2015), pp. 1035–1062, https://doi.org/10.1007/s00205-014-0805-2.

[33] E. Marušić-Paloka and I. Pažanin, *Rigorous justification of the effective boundary condition on a porous wall via homogenization*, Z. Angew. Math. Phys., 72 (2021), 146, https://doi.org/10.1007/s00033-021-01571-1.

[34] A. Mikelic, G. Guidoboni, and S. Canic, *Fluid-structure interaction in a pre-stressed tube with thick elastic walls* I*: The stationary Stokes problem*, Netw. Heterog. Media, 2 (2007), pp. 397–423, https://doi.org/10.3934/nhm.2007.2.397.

[35] A. Mikelić and J. Tambača, *Derivation of a poroelastic elliptic membrane shell model*, Appl. Anal., 98 (2019), pp. 136–161, https://doi.org/10.1080/00036811.2018.1430784.

[36] A. Mikelic and M. F. Wheeler, *On the interface law between a deformable porous medium containing a viscous fluid and an elastic body*, Math. Models Methods Appl. Sci., 22 (2012), pp. 1035–1062, https://doi.org/10.1142/S0218202512500315.

[37] B. Muha and S. Canic, *Existence of a solution to a fluid-multi-layered-structure interaction problem*, J. Differential Equations, 256 (2014), pp. 658–706, https://doi.org/10.1016/j.jde.2013.09.016.

[38] J. Orlik, R. Falconi, G. Griso, and S. Wackerle, *Asymptotic behavior for textiles with loose contact*, Math. Methods Appl. Sci., 46 (2023), pp. 17082–17127, https://doi.org/10.1002/mma.9490.

[39] J. Orlik, G. Panasenko, and V. Shiryaev, *Optimization of textile-like materials via homogenization and beam approximations*, Multiscale Model. Simul., 14 (2016), pp. 637–667, https://doi.org/10.1137/15M1017193.

[40] J. Orlik, G. Panasenko, and R. Stavre, *Asymptotic analysis of a viscous fluid layer separated by a thin stiff stratified elastic plate*, Appl. Anal., 100 (2021), pp. 589–629, https://doi.org/10.1080/00036811.2019.1612051.

[41] J. Orlik, K. Pietsch, A. Fassbender, O. Sivak, and K. Steiner, *Simulation and experimental validation of spacer fabrics based on their structure and yarn's properties*, Appl. Compos. Mater., 25 (2018), pp. 709–724, https://doi.org/10.1007/s10443-018-9726-9.

[42] G. Panasenko, *Multi-Scale Modelling for Structures and Composites*, Springer, Dordrecht, Netherlands, 2005.

[43] G. Panasenko and R. Stavre, *Asymptotic analysis of a periodic flow in a thin channel with visco-elastic wall*, J. Math. Pures Appl., 85 (2006), pp. 558–579, https://doi.org/10.1016/j.matpur.2005.10.011.

[44] V. Puderbach, S. Antonyuk, R. Kirsch, and O. Lykhachova, *Flow-induced deformation of filter media-part 1: Experimental characterization and 3d simulation of the mechanical properties of filter media during perfusion*, in Proceedings of FILTECH 2022.

[45] E. Sanchez-Palencia, *Non-Homogeneous Media and Vibration Theory*, Lecture Notes in Phys. 127, Springer, Berlin, 1980.